Northumbria Research Link

Citation: Ghayesh, Mergen H. and Farokhi, Hamed (2020) Nonlinear broadband performance of energy harvesters. International Journal of Engineering Science, 147. p. 103202.

Published by: Elsevier

URL: https://doi.org/10.1016/j.ijengsci.2019.103202 <https://doi.org/10.1016/j.ijengsci.2019.103202>

This version was downloaded from Northumbria Research Link: http://nrl.northumbria.ac.uk/id/eprint/42079/

Northumbria University has developed Northumbria Research Link (NRL) to enable users to access the University's research output. Copyright © and moral rights for items on NRL are retained by the individual author(s) and/or other copyright owners. Single copies of full items can be reproduced, displayed or performed, and given to third parties in any format or medium for personal research or study, educational, or not-for-profit purposes without prior permission or charge, provided the authors, title and full bibliographic details are given, as well as a hyperlink and/or URL to the original metadata page. The content must not be changed in any way. Full items must not be sold commercially in any format or medium without formal permission of the copyright holder. The full policy is available online: http://nrl.northumbria.ac.uk/policies.html

This document may differ from the final, published version of the research and has been made available online in accordance with publisher policies. To read and/or cite from the published version of the research, please visit the publisher's website (a subscription may be required.)

Northumbria University NEWCASTLE

University Library

Nonlinear broadband performance of energy harvesters

Mergen H. Ghayesh [a,*], Hamed Farokhi [b]

[a] *School of Mechanical Engineering, University of Adelaide, South Australia 5005, Australia*
[b] *Department of Mechanical and Construction Engineering, Northumbria University, Newcastle upon Tyne NE1 8ST, UK*
**Corresponding author: mergen.ghayesh@adelaide.edu.au*
Email: (H Farokhi): hamed.farokhi@northumbria.ac.uk

Abstract

Broadband nonlinear energy harvesting capabilities of a parametrically excited bimorph piezoelectric energy harvester is investigated for the first time. The performance of the energy harvester is significantly enhanced via use of stoppers and an added tip mass in conjunction with parametric excitation. A fully nonlinear electromechanical model of the energy harvester was developed using beam theory of Euler-Bernoulli and the coupled constitutive equations for piezoelectric materials, with the motion constraints modelled as nonlinear springs. A multi-modal discretisation was conducted utilising the Galerkin scheme; the resultant set of equations was examined numerically through use of continuation technique. It is shown that a resonance bandwidth of 46% (normalised with respect to parametric resonance frequency) is achieved which is almost 10 times the resonance bandwidth of the system without any constraints.

Keywords: Energy harvester; Wide resonance bandwidth; Nonlinear; Parametric excitation

1. Introduction

Vibration-based energy harvesters are devices which capture random environmental vibrations and harvest this otherwise wasted energy [1-7]. The harvested energy can be effectively utilised to power wireless electronics/sensors in an attempt to make these electronics devices self-powered. One of the main concerns about the efficiency of the vibration based energy harvesters is that they work efficiently only for a very narrow band of frequency, which in turn makes these devices unusable if the environmental vibration frequency does not lie within that band. A lot of research has been conducted on improving this limitation of the vibration based energy harvesters; vibration characteristics of the core elements of these systems (i.e. structures in macro/micro/nano scales [8-28]) affect the performance substantially--size effects [29-40] are also important when these structures are at micro/nano scales [41-46]. Nonlinearity of both geometric/material types [47-49] also highly influence the system performance. The literature review is briefed in the following; for more detailed reviews of the state of vibration based energy harvesters, the readers are referred to Refs. [50-54].

A micro electromagnetic power generator design was proposed by Beeby et al. [55], targeting low ambient vibrations through use of discrete components. Design consideration for piezoelectric energy harvesters for micro sensors were presented by Dutoit et al. [56]. Soliman et al. [57] proposed an electromagnetic energy harvester design by using a piecewise-linear oscillator and conducted theoretical and experimental investigations. The analysis and design of a an energy harvester working based on magnetic levitation were conducted by Mann and Sims [58], who utilised a single-mode duffing-type model to study the response of the system and compare to experimental observations. The steady state

solutions of a linear single mode model of a bimorph piezoelectric energy harvester were derived by Erturk and Inman [59]; they conducted experiments and compared the theoretical findings with experimental observations and reported acceptable agreement between the two. Kim et al. [60] utilised a single-mode linear model to examine the effects of an added tip mass on performance of an energy harvester.

The investigations were continued by Nguyen and Halvorsen [61], who analysed the effect of softening springs on performance of a micro vibration energy harvester; they concluded that the performance is enhanced when the input frequency is in the range of the softening response frequency. Ju et al. [62] developed an energy harvester utilising a magnetoelectric composite and an added tip mass made of permanent magnet. Further investigations were conducted by Firoozy et al. [63], who utilised one DOF nonlinear model to examine the energy harvesting characteristics of a piezoelectric energy harvester with a tip magnet under harmonic base excitation, and Zhao and Yang [64], who proposed an energy harvester for capturing energy from both wind flows and base vibrations using a mechanical constraint.

This study proposes, for the first time, a model for a parametrically excited broadband energy harvester subject to motion constraints taking into account all nonlinearities associated with geometry and inertia while using a multi-modal discretised model. The voltage and power outputs of the proposed designs of the energy harvester are reported for various cases. The numerical results show that a significant enhancement in the resonance bandwidth is achieved via use of motion constraints for the parametrically excited energy harvester. Additionally, it is shown that it is absolutely essential to retain all

nonlinear terms arising from geometry and inertia so as to obtain the energy harvester behaviour accurately.

2. Energy harvester nonlinear electromechanical model

The nonlinear electromechanical coupled model of the parametrically excited bimorph energy harvester is developed in this section. The nonlinear beam theory of Euler-Bernoulli [65, 66] is utilised while assuming an inextensible centreline for the cantilever, taking into account nonlinearities arising from geometry and inertia. The piezoelectric constitutive equations are used as well to obtain the coupled electromechanical equations of the bimorph piezoelectric cantilever. The schematic of the energy harvester subject to motions constraints is shown in Fig. 1. To develop a general model, it is assumed that PZT (lead zirconate titanate) layers partially cover the substrate. As seen, the width of substrate and piezoelectric layers are the same, and denoted by b. The substrate length is shown by L while PZT layers are of length $l_2^{(p)} - l_1^{(p)}$. The system is under a base motion in the form of $x_b \sin(\omega_b t)$ in the axial direction x. For a bimorph piezoelectric cantilever with same PZT layers' thickness and material, the neutral axil of the layered cantilever beam is not changed. This allows for writing the axial strain developed in substrate and PZT layers, using the inextensibility condition, as

$$\varepsilon_1 = -z\left[\left(\frac{\partial^2 w}{\partial x^2}\right) + \frac{1}{2}\left(\frac{\partial^2 w}{\partial x^2}\right)\left(\frac{\partial w}{\partial x}\right)^2\right], \tag{1}$$

in which w represents the displacement in the transverse direction, z, and subscript 1 indicates the x direction. Using Eq. (1), the substrate axial stress can be formulated as

$\sigma_s = E_s \varepsilon_1$, with E_s denoting substrate's Young's modulus. The constitutive equations for the two PZT layers are given by

$$\begin{cases} \sigma_p^{(n)} = c_{11}^{(n)} \varepsilon_1^{(n)} - h_{31}^{(n)} D_3^{(n)}, \\ E_3^{(n)} = -h_{31}^{(n)} \varepsilon_1^{(n)} + \beta_{33}^{(n)} D_3^{(n)}, \end{cases} \qquad n = 1,2, \tag{2}$$

where the top and bottom piezoelectric layers equations are obtained by setting n equal to 1 and 2, respectively; the subscripts 1 and 3 indicate the x and z directions, respectively. $c_{11}^{(n)}$ is the PZT elastic stiffness, $\beta_{33}^{(n)}$ is the impermittivity constant, and $h_{31}^{(n)}$ is another PZT constant which will be obtained later. $\sigma_p^{(n)}$ is the axial stress developed in PZT layers while $D_3^{(n)}$ and $E_3^{(n)}$ are the electric displacement and the electric field in the z direction, respectively. It should be noted that for both PZT layers, the poling direction for both is assumed to be in the positive z direction. Voltages $V^{(1)}$ and $V^{(2)}$ are generated on the PZT layers on top and bottom surfaces, respectively, due to base excitation. The virtual electrical work of these voltages is expressed as

$$\delta W_{el} = b \int_0^L \left[\left(V^{(2)}(x,t) \right) \delta D_3^{(2)} - \left(V^{(1)}(x,t) \right) \delta D_3^{(1)} \right] \mathrm{d}x. \tag{3}$$

The total kinetic energy of the layered cantilever under base excitation $x_b \sin(\omega_b t)$ is given by

$$\begin{aligned} K_e &= \int_0^L m(x) \left\{ \left[\frac{\partial}{\partial t} \left(x_b \sin(\omega_b t) - \frac{1}{2} \int_0^x \left(\frac{\partial w}{\partial x} \right)^2 \mathrm{d}x \right) \right]^2 + \left(\frac{\partial w}{\partial t} \right)^2 \right\} \mathrm{d}x, \\ m(x) &= \rho_s A_s + 2G(x) \rho_p A_p + \delta_D (x - L) M_0, \end{aligned} \tag{4}$$

in which ρ_p and ρ_s denote the mass density of the PZT layers and substrate, respectively, while A_p and A_s represent the cross-sectional area of the PZT layers and substrate,

respectively. δ_D stands for the Dirac delta function and M_0 denotes the tip mass. Additionally, $G(x)=H\left(x-l_1^{(p)}\right)-H\left(x-l_2^{(p)}\right)$, with H denoting the Heaviside function.

The variation of the substrate strain energy is formulated as

$$\delta\Pi_s=\int_0^L\int_{A_s}E_s\varepsilon_1\delta\varepsilon_1\,\mathrm{d}A\mathrm{d}x=\int_0^L\left\{E_sI_s\frac{\partial^2 w}{\partial x^2}\left[1+\frac{1}{2}\left(\frac{\partial w}{\partial x}\right)^2\right]\delta\left[\frac{\partial^2 w}{\partial x^2}\left(1+\frac{1}{2}\left(\frac{\partial w}{\partial x}\right)^2\right)\right]\right\}\mathrm{d}x, \tag{5}$$

in which I_s represents the second moment area of the substrate cross-section. The variations of the PZT layers' strain energies are formulated as

$$\begin{aligned}\delta\left(\Pi_p^{(1)}\right)&=\int_{l_1^{(p)}}^{l_2^{(p)}}\int_{A_p^{(1)}}\left[\sigma_p^{(1)}\delta\varepsilon_1+E_3^{(1)}\delta D_3^{(1)}\right]\mathrm{d}A\mathrm{d}x=\beta_{33}A_p\int_{l_1^{(p)}}^{l_2^{(p)}}D_3^{(1)}\delta D_3^{(1)}\,\mathrm{d}x\\&+\frac{1}{2}\left(t_s+t_p\right)h_{31}A_p\int_{l_1^{(p)}}^{l_2^{(p)}}\left\{\left[\frac{\partial^2 w}{\partial x^2}+\frac{1}{2}\left(\frac{\partial w}{\partial x}\right)^2\frac{\partial^2 w}{\partial x^2}\right]\delta D_3^{(1)}+D_3^{(1)}\delta\left[\frac{\partial^2 w}{\partial x^2}+\frac{1}{2}\left(\frac{\partial w}{\partial x}\right)^2\frac{\partial^2 w}{\partial x^2}\right]\right\}\mathrm{d}x\\&+\frac{1}{3}c_{11}b\left[\left(t_p\right)^3+3\left(t_p\right)^2\left(\frac{t_s}{2}\right)+3t_p\left(\frac{t_s}{2}\right)^2\right]\int_{l_1^{(p)}}^{l_2^{(p)}}\left[\frac{\partial^2 w}{\partial x^2}+\frac{1}{2}\left(\frac{\partial^2 w}{\partial x^2}\right)\left(\frac{\partial w}{\partial x}\right)^2\right]\delta\left[\frac{1}{2}\left(\frac{\partial^2 w}{\partial x^2}\right)\left(\frac{\partial w}{\partial x}\right)^2+\frac{\partial^2 w}{\partial x^2}\right]\mathrm{d}x\end{aligned} \tag{6}$$

$$\begin{aligned}\delta\Pi_p^{(2)}&=\int_{l_1^{(p)}}^{l_2^{(p)}}\int_{A_p^{(2)}}\left[\sigma_p^{(2)}\delta\varepsilon_1+E_3^{(2)}\delta D_3^{(2)}\right]\mathrm{d}A\mathrm{d}x=\beta_{33}A_p\int_{l_1^{(p)}}^{l_2^{(p)}}D_3^{(2)}\delta D_3^{(2)}\,\mathrm{d}x\\&-\frac{1}{2}\left(t_s+t_p\right)h_{31}A_p\int_{l_1^{(p)}}^{l_2^{(p)}}\left\{\left[\frac{\partial^2 w}{\partial x^2}+\frac{1}{2}\left(\frac{\partial w}{\partial x}\right)^2\frac{\partial^2 w}{\partial x^2}\right]\delta D_3^{(2)}+D_3^{(2)}\delta\left[\frac{\partial^2 w}{\partial x^2}+\frac{1}{2}\left(\frac{\partial w}{\partial x}\right)^2\frac{\partial^2 w}{\partial x^2}\right]\right\}\mathrm{d}x+\\&\frac{1}{3}c_{11}b\left[\left(t_p\right)^3+3\left(t_p\right)^2\left(\frac{t_s}{2}\right)+3t_p\left(\frac{t_s}{2}\right)^2\right]\int_{l_1^{(p)}}^{l_1^{(p)}}\left[\frac{\partial^2 w}{\partial x^2}+\frac{1}{2}\left(\frac{\partial w}{\partial x}\right)^2\frac{\partial^2 w}{\partial x^2}\right]\delta\left[\frac{\partial^2 w}{\partial x^2}+\frac{1}{2}\left(\frac{\partial^2 w}{\partial x^2}\right)\left(\frac{\partial w}{\partial x}\right)^2\right]\mathrm{d}x\end{aligned} \tag{7}$$

Using generalised Hamilton's principle, the following coupled equations are obtained

$$m(x)\frac{\partial^2 w}{\partial t^2}+\frac{\partial}{\partial x}\left\{\frac{\partial w}{\partial x}\int_L^x m(x)\left[x_b\omega_b^2\sin(\omega_b t)+\int_0^x\left(\frac{\partial^3 w}{\partial x\partial t^2}\frac{\partial w}{\partial x}+\left(\frac{\partial^2 w}{\partial x\partial t}\right)^2\right)\mathrm{d}x\right]\mathrm{d}x\right\}$$
$$+\frac{\partial}{\partial x}\left\{\frac{1}{2}\left(\frac{\partial w}{\partial x}\right)^2\frac{\partial}{\partial x}\left[C(x)\left(\frac{\partial^2 w}{\partial x^2}\right)\right]+\frac{\partial}{\partial x}\left[C(x)\left(\frac{\partial^2 w}{\partial x^2}+\frac{1}{2}\left(\frac{\partial w}{\partial x}\right)^2\frac{\partial^2 w}{\partial x^2}\right)\right]\right\} \tag{8}$$
$$+\frac{\partial}{\partial x}\left[\frac{\partial}{\partial x}\left(h(x)D_3^{(1)}-h(x)D_3^{(2)}\right)\left(1+\frac{1}{2}\left(\frac{\partial w}{\partial x}\right)^2\right)\right]=0$$

$$\beta(x)D_3^{(1)}+h(x)\left(\frac{\partial^2 w}{\partial x^2}+\frac{1}{2}\left(\frac{\partial w}{\partial x}\right)^2\frac{\partial^2 w}{\partial x^2}\right)+bV^{(1)}(x,t)=0, \tag{9}$$

$$\beta(x)D_3^{(2)}-h(x)\left(\frac{\partial^2 w}{\partial x^2}+\frac{1}{2}\left(\frac{\partial w}{\partial x}\right)^2\frac{\partial^2 w}{\partial x^2}\right)-bV^{(2)}(x,t)=0, \tag{10}$$

in which

$$C(x)=E_sI_s+2G(x)\left\{\frac{1}{3}c_{11}b\left[(t_p)^3+3(t_p)^2\left(\frac{t_s}{2}\right)+3t_p\left(\frac{t_s}{2}\right)^2\right]\right\}$$

$$h(x)=h_{31}A_p\left[\frac{1}{2}(t_s+t_p)\right]G(x),\quad \beta(x)=A_p\beta_{33}G(x) \tag{11}$$

$$V^{(1)}(x,t)=V^{(1)}(t)G(x),\qquad V^{(2)}(x,t)=V^{(2)}(t)G(x).$$

The force exerted to the cantilever beam by the motion constraints, modelled as nonlinear springs, can be formulated as

$$F_c=\delta_D(x-L)H(|w|-g_0)\mathrm{sgn}(w)\left(k_1(|w|-g_0)+k_3(|w|-g_0)^3\right), \tag{12}$$

in which g_0 denotes the gap width, and H and sgn represent the Heaviside and sign functions, respectively.

Combining Eqs. (8)-(10), denoting the base acceleration by a_x, and taking into account the contact force of the constraints yields

$$
\begin{aligned}
& m(x)\frac{\partial^2 w}{\partial t^2}+\frac{\partial}{\partial x}\left\{\frac{\partial w}{\partial x}\int_L^x m(x)\left[a_x\sin(\omega_b t)+\int_0^x\left(\frac{\partial^3 w}{\partial x\partial t^2}\frac{\partial w}{\partial x}+\left(\frac{\partial^2 w}{\partial x\partial t}\right)^2\right)\mathrm{d}x\right]\mathrm{d}x\right\} \\
& +\frac{\partial}{\partial x}\left\{\frac{1}{2}\left(\frac{\partial w}{\partial x}\right)^2\frac{\partial}{\partial x}\left[\left(\frac{\partial^2 w}{\partial x^2}\right)\left(C(x)-\frac{2\left(h(x)\right)^2}{\beta(x)}\right)\right]\right. \\
& \qquad\left.+\frac{\partial}{\partial x}\left[\left(\frac{\partial^2 w}{\partial x^2}+\frac{1}{2}\left(\frac{\partial w}{\partial x}\right)^2\frac{\partial^2 w}{\partial x^2}\right)\left(C(x)-\frac{2\left(h(x)\right)^2}{\beta(x)}\right)\right]\right\} \\
& -\frac{\partial}{\partial x}\left\{\left(1+\frac{1}{2}\left(\frac{\partial w}{\partial x}\right)^2\right)\frac{\partial}{\partial x}\left[\frac{bh(x)}{\beta(x)}\left(V^{(1)}(x,t)+V^{(2)}(x,t)\right)\right]\right\} \\
& +\delta_D(x-L)H\left(|w|-g_0\right)\mathrm{sgn}(w)\left(k_1\left(|w|-g_0\right)+k_3\left(|w|-g_0\right)^3\right)=0.
\end{aligned}
\tag{13}
$$

To obtain the power output, an electrical circuit equation is needed to couple the motion of the bimorph system to changes in the generated voltage. The generated electric current in each PZT layer can be obtained as

$$
i^{(n)}=\frac{\partial}{\partial t}\left[\int_{A_e^{(n)}}(\mathbf{D}.\mathbf{n})\mathrm{d}A\right], \qquad n=1,2, \tag{14}
$$

in which **D** represents the vector of electric displacement; **n** represents the unit vector (normal to the electrode surface area A_e). The current generated in each PZT layer can be obtained through substitution of Eqs. (9) and (10) into Eq. (14). Assuming that the electrodes cover the full surfaces of the top and bottom PZT layers, the following relations can be obtained for parallel connection of PZT layers

$$
V^{(1)}(t)=V^{(2)}(t)=V_p(t), \qquad i^{(1)}+i^{(2)}=\frac{V_p(t)}{R_l}, \tag{15}
$$

in which R_l is the load resistance in the electrical circuit. Using Eq. (15), the equation of motion, i.e. Eq. (13) can be rewritten as

$$
\begin{aligned}
& m(x)\frac{\partial^2 w}{\partial t^2}+\frac{\partial}{\partial x}\left\{\frac{\partial w}{\partial x}\int_L^x m(x)\left[a_x\sin(\omega_b t)+\int_0^x\left(\frac{\partial^3 w}{\partial x\partial t^2}\frac{\partial w}{\partial x}+\left(\frac{\partial^2 w}{\partial x\partial t}\right)^2\right)\mathrm{d}x\right]\mathrm{d}x\right\} \\
& +\frac{\partial}{\partial x}\left\{\frac{1}{2}\left(\frac{\partial w}{\partial x}\right)^2\frac{\partial}{\partial x}\left[\left(\frac{\partial^2 w}{\partial x^2}\right)\left(C(x)-\frac{2(h(x))^2}{\beta(x)}\right)\right]\right. \\
& \qquad\left.+\frac{\partial}{\partial x}\left[\left(\frac{\partial^2 w}{\partial x^2}+\frac{1}{2}\left(\frac{\partial w}{\partial x}\right)^2\frac{\partial^2 w}{\partial x^2}\right)\left(C(x)-\frac{2(h(x))^2}{\beta(x)}\right)\right]\right\} \\
& -\frac{\partial}{\partial x}\left\{\left(1+\frac{1}{2}\left(\frac{\partial w}{\partial x}\right)^2\right)\frac{\partial}{\partial x}\left[\frac{2bh(x)}{\beta(x)}V_p(t)\right]\right\} \\
& +\delta_D(x-L)H(|w|-g_0)\operatorname{sgn}(w)\left(k_1(|w|-g_0)+k_3(|w|-g_0)^3\right)=0.
\end{aligned}
\tag{16}
$$

Utilising Eqs. (9) and (10) along with Eqs. (14) and (15), one can obtain the electrical circuit equation of the bimorph cantilever energy harvester with PZT layers connected in parallel as

$$
\frac{\mathrm{d}}{\mathrm{d}t}V_p(t)+\frac{t_p\beta_{33}}{2b\left(l_2^{(p)}-l_1^{(p)}\right)}\left[\frac{V_p(t)}{R_l}+\frac{b(t_s+t_p)h_{31}}{\beta_{33}}\int_{l_1^{(p)}}^{l_2^{(p)}}\frac{\partial}{\partial t}\left(\frac{\partial^2 w}{\partial x^2}+\frac{1}{2}\left(\frac{\partial w}{\partial x}\right)^2\frac{\partial^2 w}{\partial x^2}\right)\mathrm{d}x\right]=0. \tag{17}
$$

Equations (16) and (17) represent the coupled nonlinear electromechanical continuous model of the bimorph energy harvester. In what follows, the Galerkin discretisation technique is employed to reduce the model partial differential equations into ordinary differential ones. First, the transverse displacement is defined as series expansion consisting of spatial trial functions $\Phi_n(x)$ multiplied by generalised coordinates $p_n(t)$ as

$$
w(x,t)=\sum_{n=1}^{N}\Phi_n(x)p_n(t), \tag{18}
$$

in which

$$\Phi_n(x)=\left[\cosh\left(\frac{\alpha_n x}{L}\right)-\lambda_n\sinh\left(\frac{\alpha_n x}{L}\right)\right]-\left[\cos\left(\frac{\alpha_n x}{L}\right)-\lambda_n\sin\left(\frac{\alpha_n x}{L}\right)\right],$$
$$\lambda_n=\left\{\left\{\sin(\alpha_n)+\sinh(\alpha_n)\right\}^{-1}\right\}\left\{\cos(\alpha_n)+\cosh(\alpha_n)\right\}, \tag{19}$$

in which α_n is the *n*th root the equation $1+\cos\alpha\cosh\alpha=0$. Setting *N*=6, and applying the Galerkin method [67-70] to Eq. (16) yields a set of 7 nonlinearly coupled equations. It should be noted that in this study, a modal damping mechanism is used to model the energy dissipation in the system. This modal damping is added to the discretised equations while assuming each mode's damping to be proportional to its natural frequency. The final discretised model consists of various sources of nonlinearity; a continuation code is developed, capable of handling all these nonlinearities, to examine the response of the energy harvester near parametric resonance.

3. Broadband energy harvesting

The energy harvesting capability of the parametrically excited bimorph piezoelectric cantilever energy harvester is studied in this section. The dimensions and mechanical properties of the energy harvester examined in this study are detailed in Table 1, which allows for calculating the following piezoelectric constants

$$c_{11}=\left(s_{11}-d_{31}^2/\xi_{33}\right)^{-1}=69.81\text{ GPa},$$
$$h_{31}=-\left(d_{31}-s_{11}\xi_{33}/d_{31}\right)^{-1}=-579.76\text{ MV/m}, \tag{20}$$
$$\beta_{33}=\left(\xi_{33}-d_{31}^2/s_{11}\right)^{-1}=38.03\text{ Mm/F}.$$

Throughout this section, it is assumed that $l_1^{(p)}$=0 and $l_2^{(p)}$=*L*, and that the base acceleration is 9.81 m/s^2. Additionally, a nondimensional quantity is defined as

$\gamma = M_0 / \left(\rho_s A_s L + 2\rho_p A_p L \right)$, representing the ratio of the tip mass to the total mass of both the layered beam. The following two subsections examine the behaviour of two energy harvester designs with different tip masses.

3.1 Constrained bimorph system with γ=2.0

This section examines the parametric response of an energy harvester with γ=2.0 and dimensions and properties given in Table 1. For such a harvester, the short-circuit natural frequency is obtained as 4.7564 Hz. Given that the system is under axial base excitation, parametric resonance is expected to occur for frequencies around twice the natural frequency, i.e. 9.5128 Hz. Figure 2 illustrates the nonlinear parametric response of the constrained bimorph energy harvester. As seen, two nontrivial branches bifurcate from the zero-amplitude trivial branch as the base motion frequency is varied around twice the natural frequency. Period-doubling (PD) bifurcations occur at these points rendering the trivial configuration unstable. One of the interesting features of the proposed design is the presence of motion constraints at both sides of the cantilever beam, as demonstrated in Fig. 1. For the case examined here, g_0 is set to 42 mm. As seen, in Fig. 2(a), the transverse motion amplitude almost stops growing as it reaches 42 mm, signalling contact with the motion constraints; additionally, it is seen that the width of the parametric resonance band is increased significantly as a result of the impact between the cantilever and the constraints. More specifically, the resonance band is increased from 0.2068 Hz to 1.8521 Hz, i.e. an increase of almost 800%. Hence, the energy harvester displays a normalised resonance bandwidth of 20%; the normalised resonance bandwidth is the ratio between the resonance bandwidth and resonance frequency, with the latter being twice the first natural

frequency for parametric resonance. The points shown by TR and SD denote the torus and saddle-node bifurcations. The dotted line between TR points represents quasiperiodic motion while the dashed lines indicate unstable response. The power output for this broadband energy harvester is shown in Fig. 2(c). It is seen that, as the contact is initiated, the maximum power output is around 18 mW. The power output increases throughout the wide resonance band as the base frequency is increased reaching a maximum of around 27 mW. The detailed responses of the energy harvester at ω_b=10.0458 Hz and 11.2666 Hz in one periodic of oscillation are shown in Figs. 4 and 5, respectively.

The effect of the load resistance on the voltage and power outputs of the system is highlighted in Fig. 3. The widest resonance band is achieved when R_l = 1kΩ, which is almost two times the bandwidth of the case R_l = 5kΩ. Increasing the load resistance results in decreased bandwidth, but increases the power output level. Hence, choosing the load resistance magnitude is a critical task in the design of a constrained parametrically excited energy harvester. In particular, the choice of the resonance load is a trade-off between resonance band and power output level. The optimum value of the load resistance depends on the type of energy harvester and its usage as well as the environmental vibration range.

The gap width effect on resonance response of the bimorph energy harvester is depicted in Fig. 6. As seen, the resonance bandwidth of the voltage and power outputs decreases slightly with increasing gap width; however, the voltage and power output levels increase with increasing gap width. Hence, theoretically, a larger gap width is beneficial as it results is larger power output levels while not sacrificing the resonance bandwidth much.

Figure 7 shows a comparison between the voltage and power outputs of a bimorph energy harvester constrained from both sides to those of the same harvester constrained

from one side (i.e. the top). As seen, the resonance bandwidth is much larger for the case constrained from both sides. Hence, the conclusion may be drawn that a double-sided constrained energy harvester has better efficiency compared to a one-sided constrained energy harvester.

3.2 Constrained bimorph system with γ=3.0

The performance of a parametrically excited energy harvester with γ=3.0 is examined in this section; the rest of the system parameters remain unchanged compared to Section 3.1. Due to increased tip mass ratio, short-circuit natural frequency decreases to 3.9541 Hz compared to 4.7564 Hz of the system of Section 3.1. As a result, the parametric resonance occurs in the vicinity of base frequency of 7.9081 Hz. Figure 8 shows the parametric resonance responses of the constrained energy harvester for tip transverse displacement, voltage output, and hence the power output. The energy harvester performance is enhanced significantly through widened resonance bandwidth due to presence of motion constraints. To put it into numbers, the presence of motion constraints increases the bandwidth from 0.3642 Hz to 3.6302 Hz, i.e. an increase of almost 900%. The normalised resonance bandwidth for this case is obtained as 46%. Additionally, compared to the case of the system of Fig. 2 with γ=2.0 and a resonance bandwidth of 1.8521 Hz, a 96% increase in the bandwidth is achieved. Additionally, it is seen that the power output levels vary in the range 23 mW to almost 40 mW which is higher than the power output level of the system of Section 3.1. Another change that can be observed compared to the case of the previous section is the increased number of regions showing quasiperiodic motion. The energy harvester displacement, voltage and power outputs in one period of oscillation at

ω_b=8.3700 Hz and 11.3634 are depicted in Figs. 9 and 10. The impact behaviour of the system is very visible in Fig. 10.

The effect of the load resistance on the voltage/power outputs of the bimorph piezoelectric energy harvester is illustrate in Fig. 11. The figure shows that as the load resistance is increased from 5 kΩ to 8 kΩ, the voltage and power outputs increase accordingly while the resonance bandwidth decreases slightly. As the load resistance is further increased from 8 kΩ to 11 kΩ, a similar increase in the power output is observed but at the cost of reduced bandwidth; a similar behaviour is observed by increasing the load resistance further to 15 kΩ. Hence, the resonance bandwidth and the power output level are competing objectives; the optimum load resistance can be obtained by giving appropriate weights to resonance bandwidth and power output level and then maximising the weighted summation of both.

The effect of the gap width on voltage and power outputs of the parametrically excited constrained energy harvester is depicted in Fig. 12. Similar to the case of the previous section, it is seen that increasing the gap width has almost no effect on the resonance bandwidth; however, the power output is significantly increased as the gap width is increased from 27 mm to 45 mm. Hence from theoretical point of view, for the current energy harvester design, the performance can be enhanced by increasing the gap width.

A comparison between an energy harvester constrained from both sides to another harvester constrained from one side is shown in Fig. 13. As seen, the resonance bandwidth is reduced almost 50% as the number of constraints is reduced from two to one. Hence, the figure clearly shows that an energy harvester design with constraints at both sides displays

superior efficiency in capturing the energy of a wider range of environmental vibration compared to an energy harvester constrained from only one side.

4. Conclusions

The performance of nonlinear constrained bimorph piezoelectric energy harvester under parametric excitation was studied in detail. To ensure the accuracy of the proposed theoretical model, all the nonlinear terms arising from geometry, inertia, and contact with motion constraints were retained while deriving the coupled electromechanical equations.

Two designs were proposed for an energy harvester capturing the energy of base parametric motions. To enhance the efficiency of the energy harvesters, motion constraints were placed at both sides of the bimorph piezoelectric cantilever. It was shown that the performance of both energy harvesters were enhanced significantly through widened resonance bandwidth. More specifically, the first design with γ=2.0 achieved a normalised resonance bandwidth of 20% while this value was increased to 46% for the second design with γ=3.0. Compared to the cases without any constraints, the addition of motion constraints increased the resonance bandwidth by 800% for the first design and almost 900% for the second design.

The effect of various parameters on energy harvester performance and efficiency was examined and the following conclusions were drawn: (i) increasing the load resistance magnitude results in increased power output levels but decreases the resonance bandwidth; (ii) as the gap width is increased, the power output increases as well while the resonance bandwidth remains almost the same; (iii) removing one of the constraints, i.e.

constraining the system from only one side, results in significantly reduced bandwidth, i.e. almost 50%.

Appendix A. Effect of sources of nonlinearity

Figure 14 depicts the nonlinear frequency curve of the tip transverse displacement of the bimorph cantilever based on various models, namely a complete nonlinear model (i.e. the one used in this study), a nonlinear model retaining only geometric nonlinearities, a nonlinear model retaining only inertial nonlinearities, and a linear model. It is seen that geometric nonlinear terms tend to have a hardening effect on frequency response of the system while inertial nonlinear terms have a softening effect on the system's resonance response. In is interesting to note that a linear model is incapable of anticipating the system behaviour beyond the trivial zero-amplitude solution branch. This shows the significant importance of employing a fully nonlinear model when examining the response of a bimorph piezoelectric cantilever energy harvester under parametric excitations.

References

[1] R. Basutkar, Analytical modelling of a nanoscale series-connected bimorph piezoelectric energy harvester incorporating the flexoelectric effect, International Journal of Engineering Science, 139 (2019) 42-61.

[2] N. Tran, M.H. Ghayesh, M. Arjomandi, Ambient vibration energy harvesters: A review on nonlinear techniques for performance enhancement, International Journal of Engineering Science, 127 (2018) 162-185.

[3] M. Rezaei, S.E. Khadem, P. Firoozy, Broadband and tunable PZT energy harvesting utilizing local nonlinearity and tip mass effects, International Journal of Engineering Science, 118 (2017) 1-15.

[4] K.F. Wang, B.L. Wang, Non-linear flexoelectricity in energy harvesting, International Journal of Engineering Science, 116 (2017) 88-103.

[5] P. Firoozy, S.E. Khadem, S.M. Pourkiaee, Broadband energy harvesting using nonlinear vibrations of a magnetopiezoelastic cantilever beam, International Journal of Engineering Science, 111 (2017) 113-133.

[6] X. Xie, Q. Wang, A mathematical model for piezoelectric ring energy harvesting technology from vehicle tires, International Journal of Engineering Science, 94 (2015) 113-127.

[7] X.D. Xie, N. Wu, K.V. Yuen, Q. Wang, Energy harvesting from high-rise buildings by a piezoelectric coupled cantilever with a proof mass, International Journal of Engineering Science, 72 (2013) 98-106.

[8] M.H. Jalaei, A.G. Arani, H. Tourang, On the dynamic stability of viscoelastic graphene sheets, International Journal of Engineering Science, 132 (2018) 16-29.

[9] L. Lu, X. Guo, J. Zhao, On the mechanics of Kirchhoff and Mindlin plates incorporating surface energy, International Journal of Engineering Science, 124 (2018) 24-40.

[10] T. Natsuki, J. Natsuki, Transverse impact analysis of double-layered graphene sheets on an elastic foundation, International Journal of Engineering Science, 124 (2018) 41-48.

[11] H. Shahverdi, M.R. Barati, Vibration analysis of porous functionally graded nanoplates, International Journal of Engineering Science, 120 (2017) 82-99.

[12] R. Barretta, S.A. Faghidian, F. Marotti de Sciarra, Stress-driven nonlocal integral elasticity for axisymmetric nano-plates, International Journal of Engineering Science, 136 (2019) 38-52.

[13] M.A. Attia, A.A. Abdel Rahman, On vibrations of functionally graded viscoelastic nanobeams with surface effects, International Journal of Engineering Science, 127 (2018) 1-32.

[14] R. Barretta, M. Čanađija, R. Luciano, F.M. de Sciarra, Stress-driven modeling of nonlocal thermoelastic behavior of nanobeams, International Journal of Engineering Science, 126 (2018) 53-67.

[15] B. Karami, M. Janghorban, On the dynamics of porous nanotubes with variable material properties and variable thickness, International Journal of Engineering Science, 136 (2019) 53-66.

[16] H.B. Khaniki, On vibrations of nanobeam systems, International Journal of Engineering Science, 124 (2018) 85-103.

[17] L. Li, H. Tang, Y. Hu, The effect of thickness on the mechanics of nanobeams, International Journal of Engineering Science, 123 (2018) 81-91.

[18] H.B. Khaniki, On vibrations of FG nanobeams, International Journal of Engineering Science, 135 (2019) 23-36.

[19] G.-L. She, Y.-R. Ren, F.-G. Yuan, W.-S. Xiao, On vibrations of porous nanotubes, International Journal of Engineering Science, 125 (2018) 23-35.

[20] H. Farokhi, M.H. Ghayesh, A. Gholipour, S. Hussain, Motion characteristics of bilayered extensible Timoshenko microbeams, International Journal of Engineering Science, 112 (2017) 1-17.

[21] M.H. Ghayesh, H. Farokhi, A. Gholipour, Oscillations of functionally graded microbeams, International Journal of Engineering Science, 110 (2017) 35-53.

[22] M.H. Ghayesh, H. Farokhi, A. Gholipour, Vibration analysis of geometrically imperfect three-layered shear-deformable microbeams, International Journal of Mechanical Sciences, 122 (2017) 370-383.

[23] H. Farokhi, M.H. Ghayesh, Nonlinear mechanics of electrically actuated microplates, International Journal of Engineering Science, 123 (2018) 197-213.
[24] M.H. Ghayesh, H. Farokhi, A. Gholipour, M. Tavallaeinejad, Nonlinear oscillations of functionally graded microplates, International Journal of Engineering Science, 122 (2018) 56-72.
[25] H. Farokhi, M.H. Ghayesh, On the dynamics of imperfect shear deformable microplates, International Journal of Engineering Science, 133 (2018) 264-283.
[26] M.H. Ghayesh, S. Kazemirad, M.A. Darabi, A general solution procedure for vibrations of systems with cubic nonlinearities and nonlinear/time-dependent internal boundary conditions, Journal of Sound and Vibration, 330 (2011) 5382-5400.
[27] M.H. Ghayesh, S. Kazemirad, T. Reid, Nonlinear vibrations and stability of parametrically exited systems with cubic nonlinearities and internal boundary conditions: A general solution procedure, Applied Mathematical Modelling, 36 (2012) 3299-3311.
[28] M.H. Ghayesh, M. Amabili, H. Farokhi, Coupled global dynamics of an axially moving viscoelastic beam, International Journal of Non-Linear Mechanics, 51 (2013) 54-74.
[29] F. Ebrahimi, M.R. Barati, A. Dabbagh, A nonlocal strain gradient theory for wave propagation analysis in temperature-dependent inhomogeneous nanoplates, International Journal of Engineering Science, 107 (2016) 169-182.
[30] L. Lu, X. Guo, J. Zhao, Size-dependent vibration analysis of nanobeams based on the nonlocal strain gradient theory, International Journal of Engineering Science, 116 (2017) 12-24.
[31] M. Şimşek, Nonlinear free vibration of a functionally graded nanobeam using nonlocal strain gradient theory and a novel Hamiltonian approach, International Journal of Engineering Science, 105 (2016) 12-27.
[32] X. Zhu, L. Li, Closed form solution for a nonlocal strain gradient rod in tension, International Journal of Engineering Science, 119 (2017) 16-28.
[33] S.A. Faghidian, Integro-differential nonlocal theory of elasticity, International Journal of Engineering Science, 129 (2018) 96-110.
[34] J. Fernández-Sáez, R. Zaera, Vibrations of Bernoulli-Euler beams using the two-phase nonlocal elasticity theory, International Journal of Engineering Science, 119 (2017) 232-248.
[35] G. Romano, R. Barretta, Nonlocal elasticity in nanobeams: the stress-driven integral model, International Journal of Engineering Science, 115 (2017) 14-27.
[36] A. Apuzzo, R. Barretta, S.A. Faghidian, R. Luciano, F. Marotti de Sciarra, Free vibrations of elastic beams by modified nonlocal strain gradient theory, International Journal of Engineering Science, 133 (2018) 99-108.
[37] M.H. Ghayesh, M. Amabili, H. Farokhi, Three-dimensional nonlinear size-dependent behaviour of Timoshenko microbeams, International Journal of Engineering Science, 71 (2013) 1-14.
[38] M.H. Ghayesh, H. Farokhi, M. Amabili, Nonlinear dynamics of a microscale beam based on the modified couple stress theory, Composites Part B: Engineering, 50 (2013) 318-324.
[39] M.H. Ghayesh, H. Farokhi, Nonlinear dynamics of microplates, International Journal of Engineering Science, 86 (2015) 60-73.
[40] H. Farokhi, M.H. Ghayesh, Nonlinear dynamical behaviour of geometrically imperfect microplates based on modified couple stress theory, International Journal of Mechanical Sciences, 90 (2015) 133-144.
[41] R. Bahaadini, A.R. Saidi, M. Hosseini, On dynamics of nanotubes conveying nanoflow, International Journal of Engineering Science, 123 (2018) 181-196.
[42] F. Ebrahimi, M.R. Barati, A nonlocal higher-order refined magneto-electro-viscoelastic beam model for dynamic analysis of smart nanostructures, International Journal of Engineering Science, 107 (2016) 183-196.
[43] N.M. Faleh, R.A. Ahmed, R.M. Fenjan, On vibrations of porous FG nanoshells, International Journal of Engineering Science, 133 (2018) 1-14.
[44] A. Hadi, M.Z. Nejad, M. Hosseini, Vibrations of three-dimensionally graded nanobeams, International Journal of Engineering Science, 128 (2018) 12-23.

[45] L. Lu, X. Guo, J. Zhao, A unified nonlocal strain gradient model for nanobeams and the importance of higher order terms, International Journal of Engineering Science, 119 (2017) 265-277.
[46] X. Zhu, L. Li, On longitudinal dynamics of nanorods, International Journal of Engineering Science, 120 (2017) 129-145.
[47] M.H. Ghayesh, H. Farokhi, Chaotic motion of a parametrically excited microbeam, International Journal of Engineering Science, 96 (2015) 34-45.
[48] A. Gholipour, H. Farokhi, M.H. Ghayesh, In-plane and out-of-plane nonlinear size-dependent dynamics of microplates, Nonlinear Dynamics, 79 (2015) 1771-1785.
[49] M.H. Ghayesh, H. Farokhi, M. Amabili, In-plane and out-of-plane motion characteristics of microbeams with modal interactions, Composites Part B: Engineering, 60 (2014) 423-439.
[50] F.K. Shaikh, S. Zeadally, Energy harvesting in wireless sensor networks: A comprehensive review, Renewable and Sustainable Energy Reviews, 55 (2016) 1041-1054.
[51] Y. Tan, Y. Dong, X. Wang, Review of MEMS Electromagnetic Vibration Energy Harvester, Journal of Microelectromechanical Systems, 26 (2017) 1-16.
[52] D. Zhu, M.J. Tudor, S.P. Beeby, Strategies for increasing the operating frequency range of vibration energy harvesters: a review, Measurement Science and Technology, 21 (2009) 022001.
[53] Z. Wu, R. Liu, Q. Liu, M. Zhang, Dynamic characteristics of a novel bistable electromagnetic vibration energy harvester excited by gauss white noise, in: 2017 2nd International Conference on Power and Renewable Energy, ICPRE 2017, 2018, pp. 152-156.
[54] T. Yildirim, M.H. Ghayesh, W. Li, G. Alici, A review on performance enhancement techniques for ambient vibration energy harvesters, Renewable and Sustainable Energy Reviews, 71 (2017) 435-449.
[55] S.P. Beeby, R. Torah, M. Tudor, P. Glynne-Jones, T. O'donnell, C. Saha, S. Roy, A micro electromagnetic generator for vibration energy harvesting, Journal of Micromechanics and microengineering, 17 (2007) 1257.
[56] N.E. Dutoit, B.L. Wardle, S.-G. Kim, Design considerations for MEMS-scale piezoelectric mechanical vibration energy harvesters, Integrated ferroelectrics, 71 (2005) 121-160.
[57] M. Soliman, E. Abdel-Rahman, E. El-Saadany, R. Mansour, A wideband vibration-based energy harvester, Journal of Micromechanics and Microengineering, 18 (2008) 115021.
[58] B.P. Mann, N.D. Sims, Energy harvesting from the nonlinear oscillations of magnetic levitation, Journal of Sound and Vibration, 319 (2009) 515-530.
[59] A. Erturk, D.J. Inman, An experimentally validated bimorph cantilever model for piezoelectric energy harvesting from base excitations, Smart Materials and Structures, 18 (2009) 025009.
[60] M. Kim, M. Hoegen, J. Dugundji, B.L. Wardle, Modeling and experimental verification of proof mass effects on vibration energy harvester performance, Smart Materials and Structures, 19 (2010) 045023.
[61] S.D. Nguyen, E. Halvorsen, Nonlinear springs for bandwidth-tolerant vibration energy harvesting, Journal of Microelectromechanical Systems, 20 (2011) 1225-1227.
[62] S. Ju, S.H. Chae, Y. Choi, S. Lee, H.W. Lee, C.-H. Ji, A low frequency vibration energy harvester using magnetoelectric laminate composite, Smart Materials and Structures, 22 (2013) 115037.
[63] P. Firoozy, S.E. Khadem, S.M. Pourkiaee, Broadband energy harvesting using nonlinear vibrations of a magnetopiezoelastic cantilever beam, International Journal of Engineering Science, 111 (2017) 113-133.
[64] L. Zhao, Y. Yang, An impact-based broadband aeroelastic energy harvester for concurrent wind and base vibration energy harvesting, Applied Energy, 212 (2018) 233-243.
[65] M.H. Ghayesh, H. Farokhi, G. Alici, Size-dependent performance of microgyroscopes, International Journal of Engineering Science, 100 (2016) 99-111.
[66] H. Farokhi, M. Ghayesh, M. Amabili, Nonlinear dynamics of a geometrically imperfect microbeam based on the modified couple stress theory, International Journal of Engineering Science, 68 (2013) 11-23.

[67] H. Farokhi, M.H. Ghayesh, Thermo-mechanical dynamics of perfect and imperfect Timoshenko microbeams, International Journal of Engineering Science, 91 (2015) 12-33.
[68] M.H. Ghayesh, H. Farokhi, M. Amabili, Nonlinear behaviour of electrically actuated MEMS resonators, International Journal of Engineering Science, 71 (2013) 137-155.
[69] M.H. Ghayesh, M. Amabili, H. Farokhi, Nonlinear forced vibrations of a microbeam based on the strain gradient elasticity theory, International Journal of Engineering Science, 63 (2013) 52-60.
[70] H. Farokhi, M.H. Ghayesh, Supercritical nonlinear parametric dynamics of Timoshenko microbeams, Communications in Nonlinear Science and Numerical Simulation, 59 (2018) 592-605.

Table 1. Properties and dimensions of the substrate and piezoelectric layers of the bimoprph cantilever energy harvester

Properties and dimensions	Substrate (brass)	Properties and dimensions	Each PZT layer (PZT-5H)
t_s (mm)	0.3	t_p (mm)	0.2
b (mm)	20	b (mm)	20
L (mm)	150	L (mm)	150
ρ_s (kg/m^3)	8490	ρ_p (kg/m^3)	7400
E_s (GPa)	106	s_{11} (pm^2/N)	16.4
		ξ_{33}/ξ_0 (ξ_0 = 8.8542 pF/m)	3400
		d_{31} (pm/V)	-250

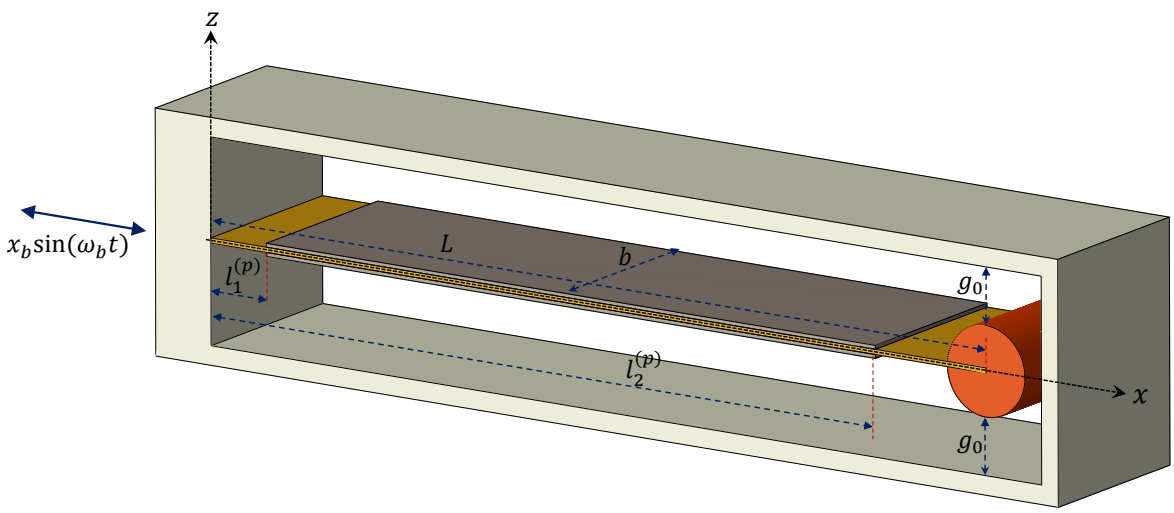

Fig.1. Schematic of the constrained bimorph piezoelectric cantilever energy harvester.

(a)

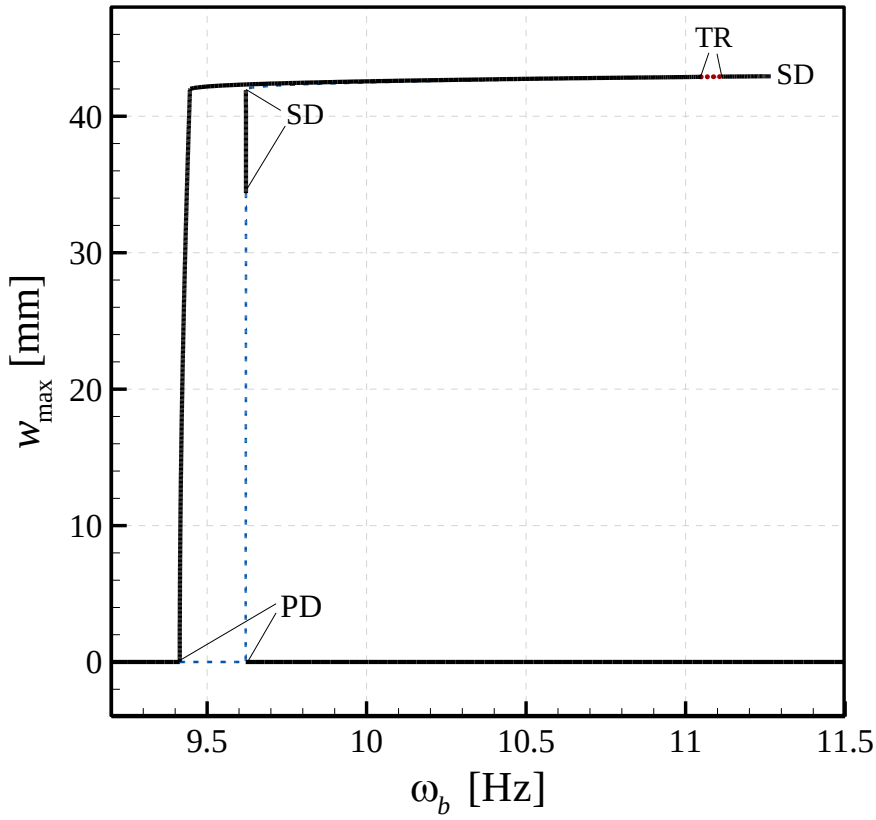
TR
SD
SD
PD
40
30
20
10
0
9.5
10
10.5
11
11.5
w_{max} [mm]
ω_b [Hz]

(b)

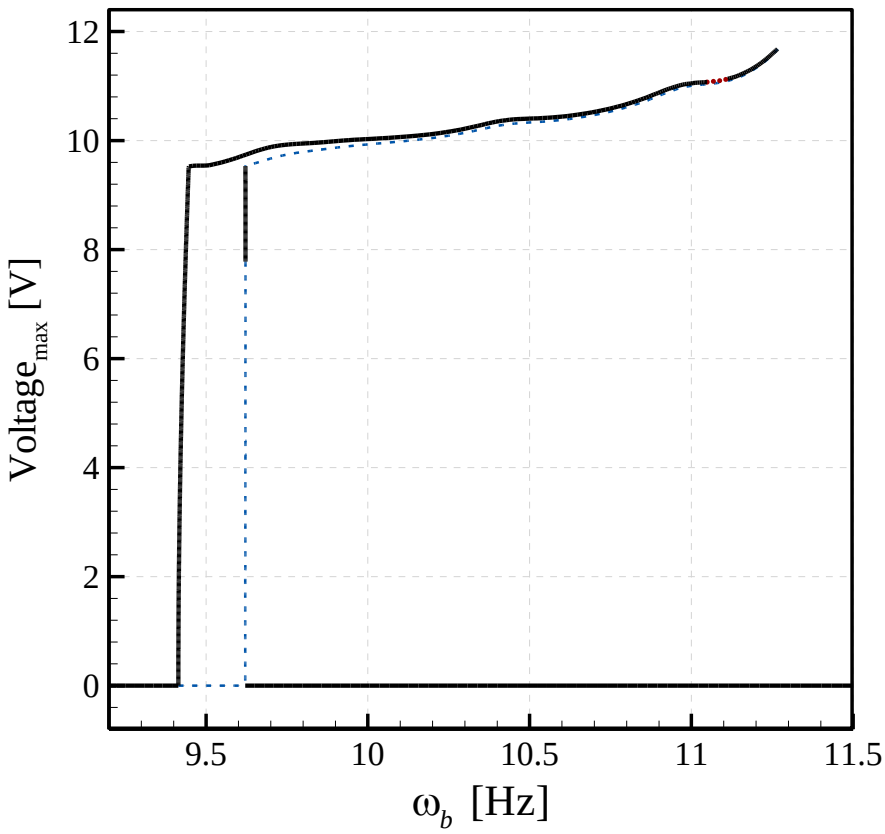
12
10
8
6
4
2
0
9.5
10
10.5
11
11.5
Voltage$_{max}$ [V]
ω_b [Hz]

(c)

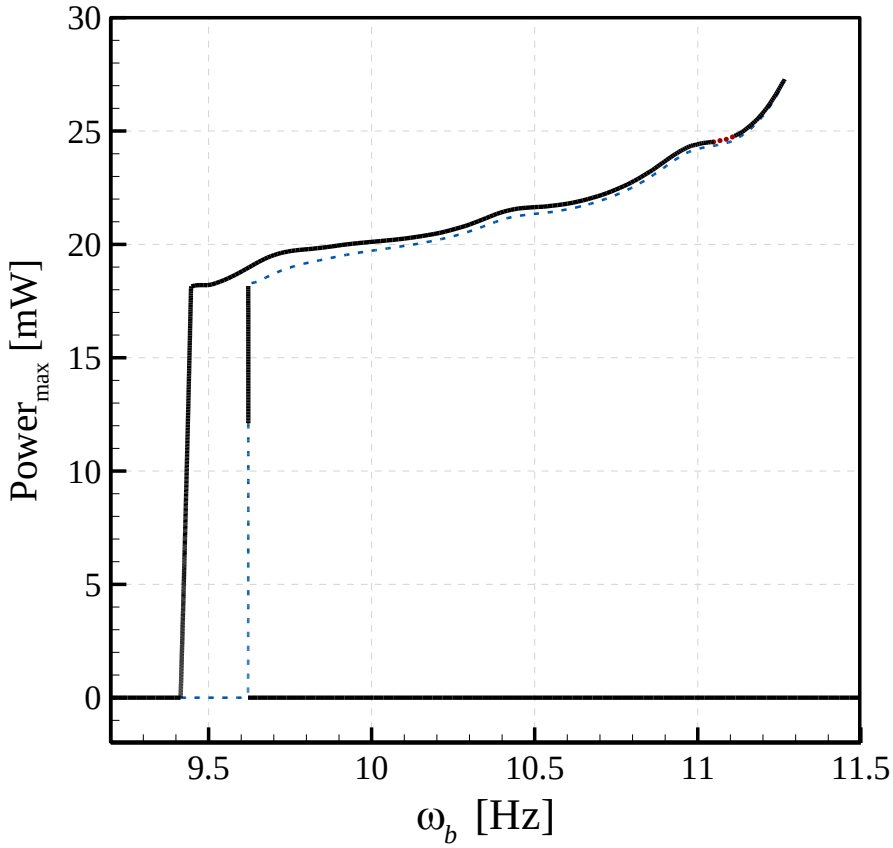

Fig.2. Frequency responses of the parametrically excited constrained bimorph cantilever energy harvester: (a) maximum tip transverse displacement; (b, c) maximum voltage and power outputs, respectively. R_l=5.0 kΩ, γ=2.0, g_0=42.0 mm, and a_x=9.81 m/s^2.

(a)

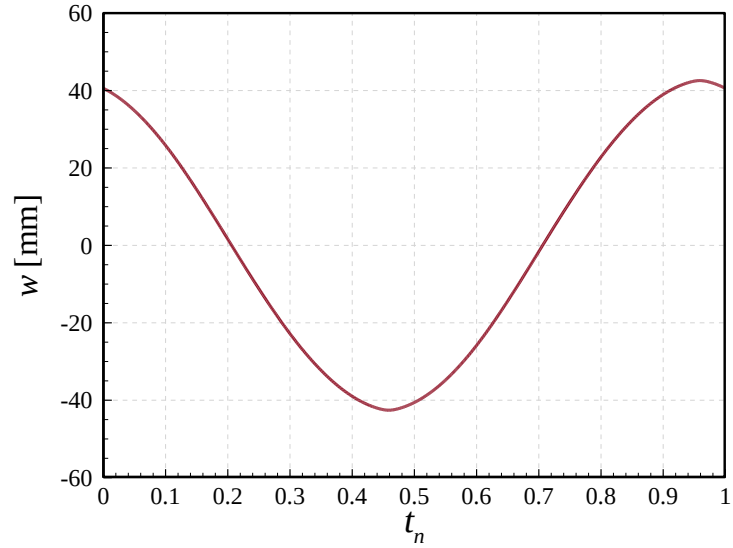

(b)

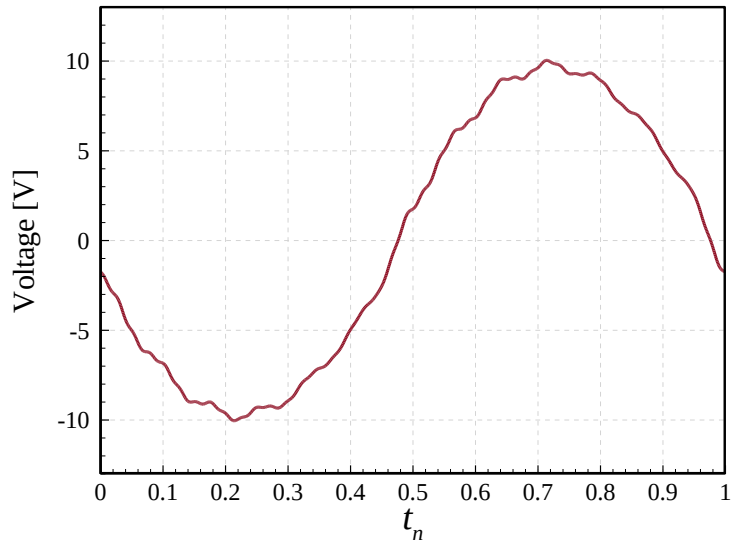

(c)

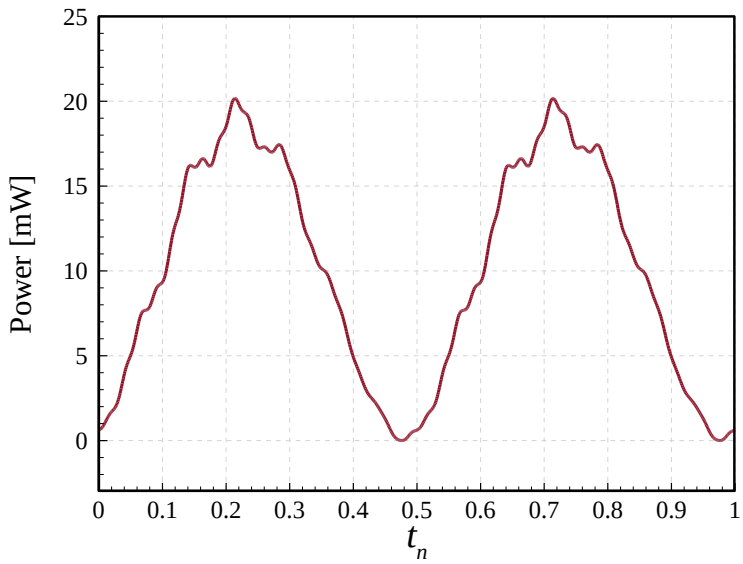

Fig.3. Response of the system of Fig. 2 at ω_b=10.0458 Hz; (a-c) tip transverse displacement, voltage output, and power output in one period of oscillation, respectively. t_n: normalised time.

(a)

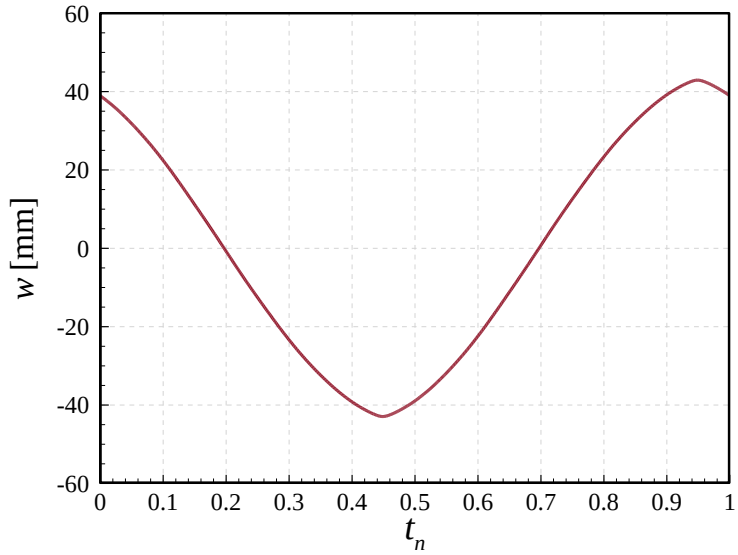

(b)

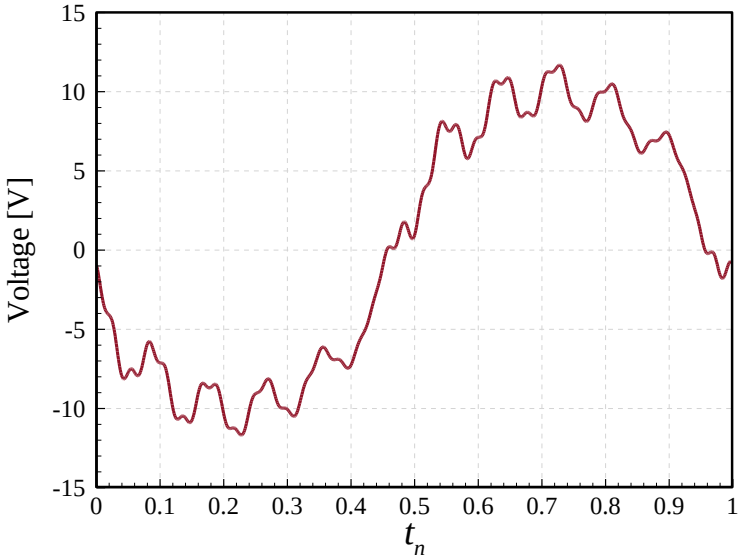

(c)

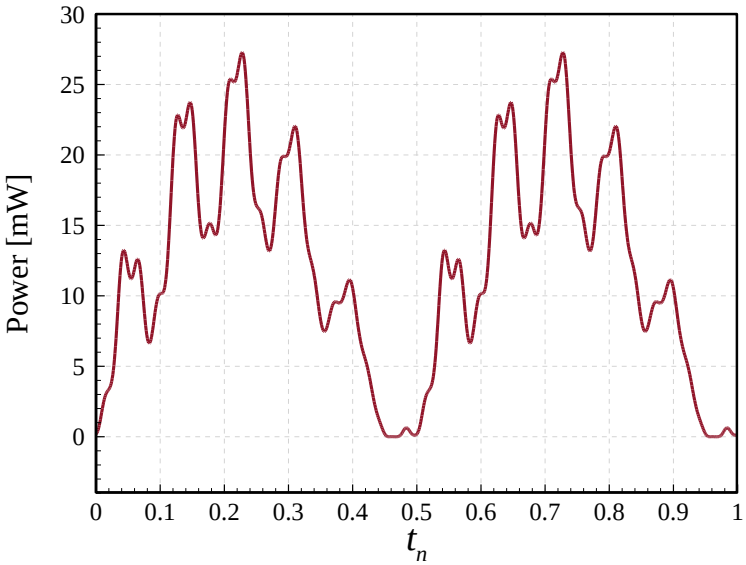

Fig.4. Response of the system of Fig. 2 at ω_b=11.2666 Hz; (a-c) tip transverse displacement, voltage output, and power output in one period of oscillation, respectively. t_n: normalised time.

(a)

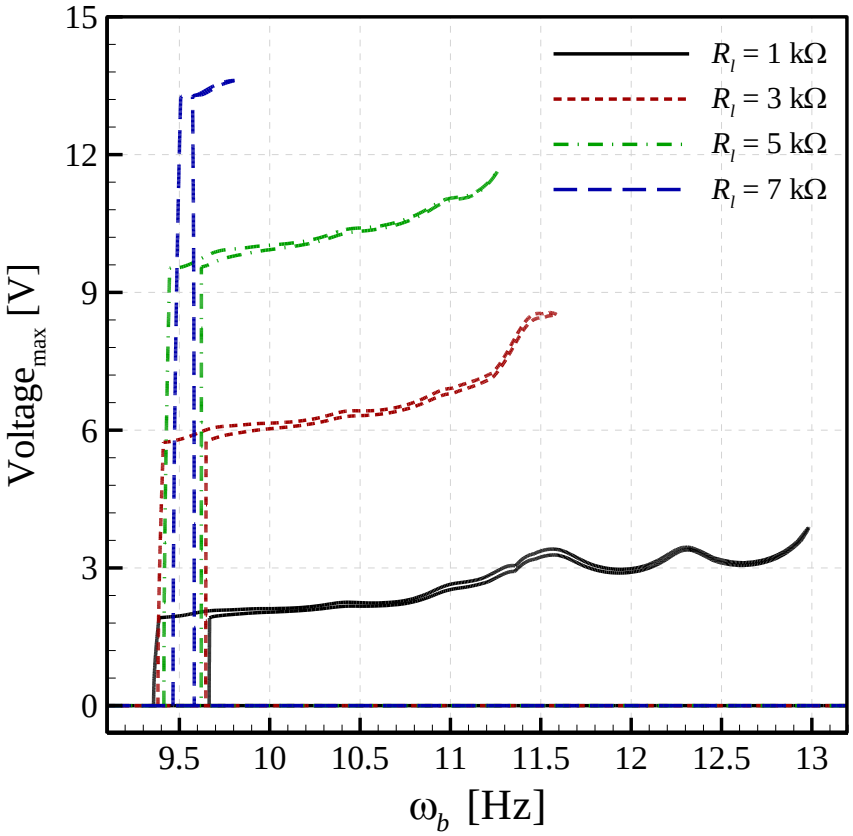

(b)

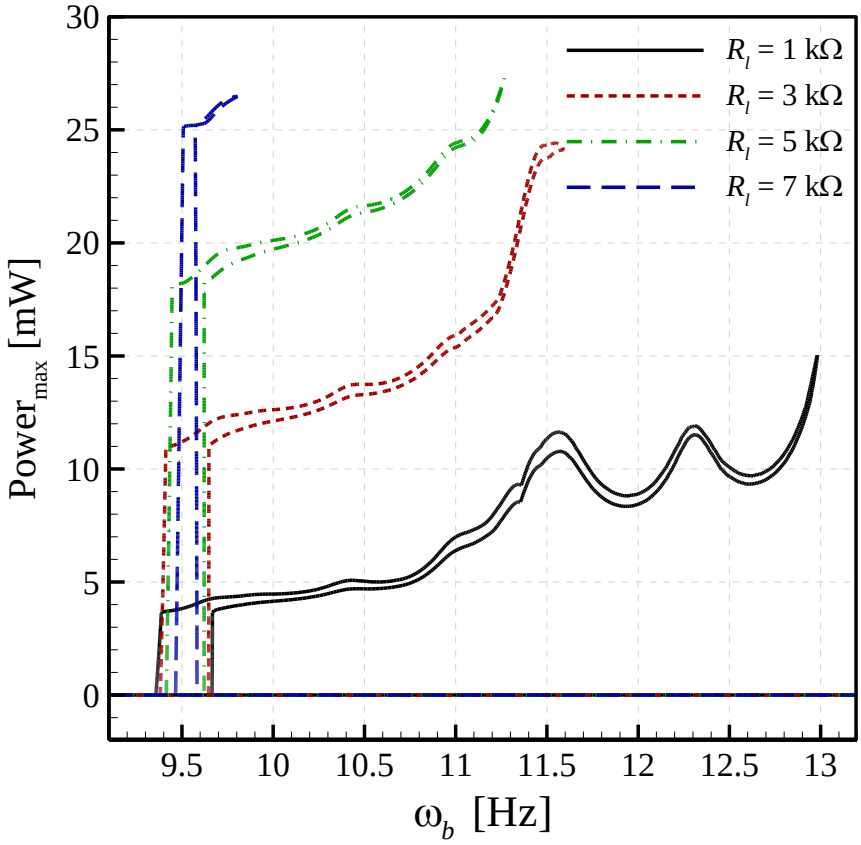

Fig.5. Load resistance effect on frequency responses of the parametrically excited constrained bimorph cantilever energy harvester: (a, b) maximum voltage and power outputs, respectively. γ=2.0, g_0=42.0 mm, and a_x=9.81 m/s^2.

(a)

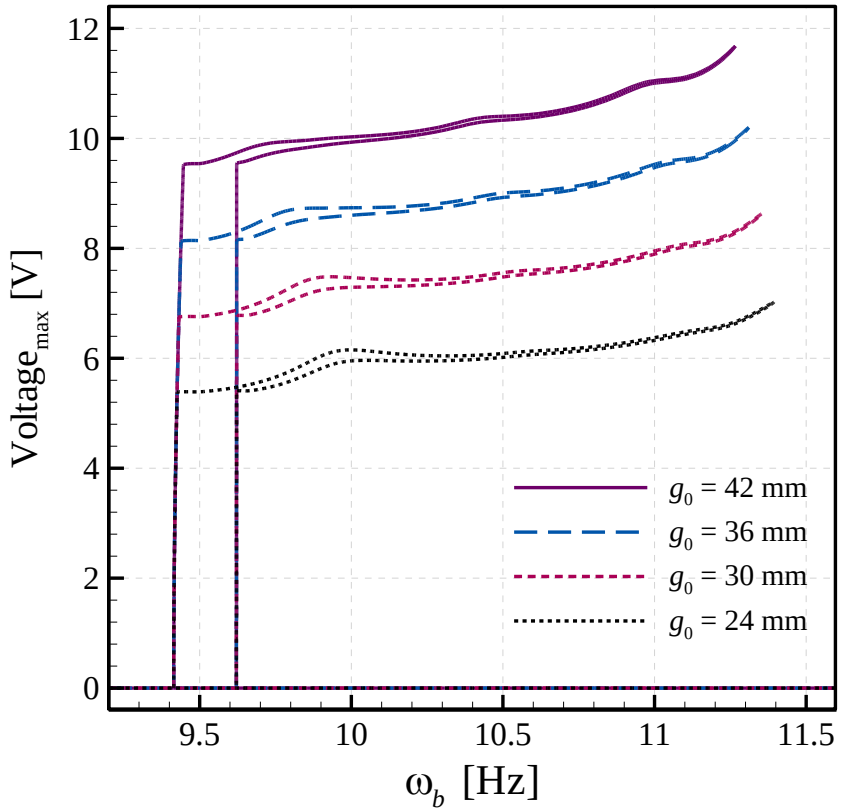

(b)

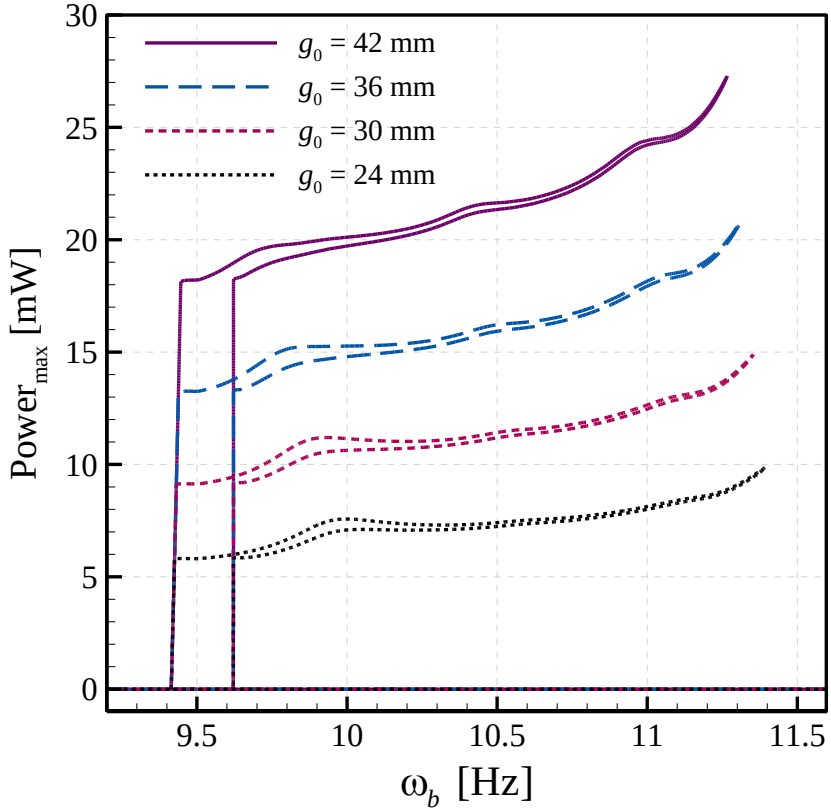

Fig.6. Gap effect on frequency responses of the parametrically excited constrained bimorph cantilever energy harvester: (a, b) maximum voltage and power outputs, respectively. R_l=5.0 kΩ, γ=2.0, and a_x=9.81 m/s^2.

(a)

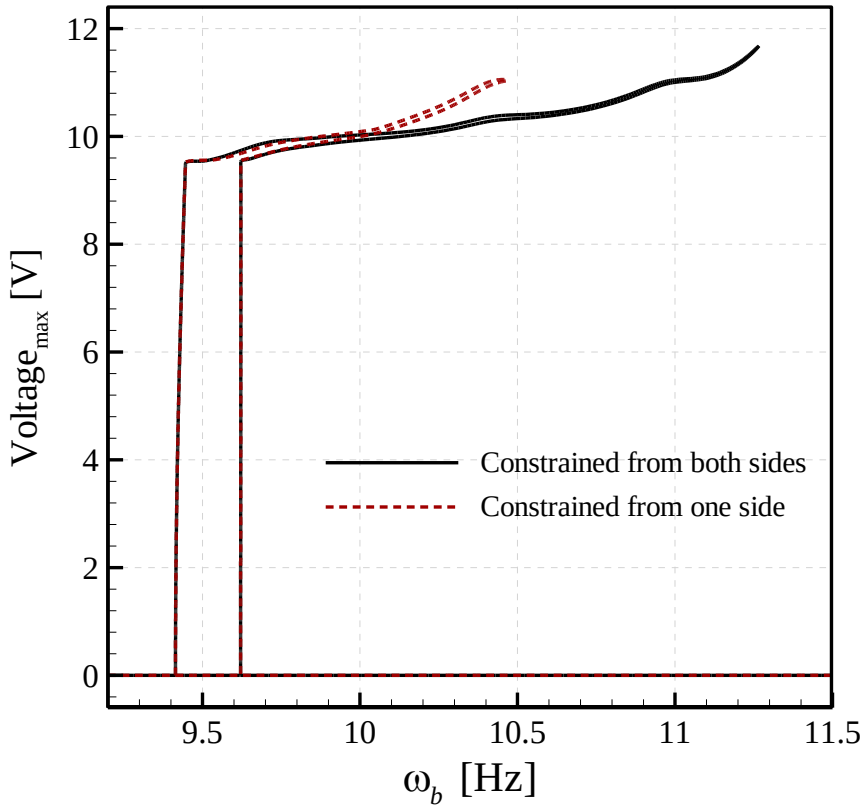

(b)

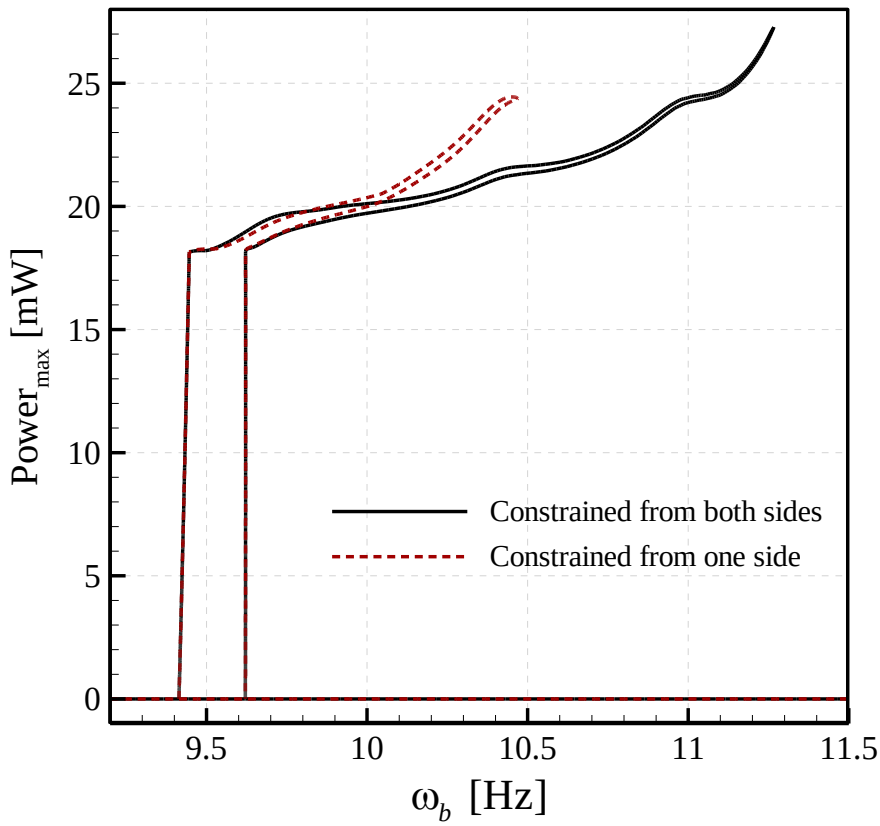

Fig.7. Frequency responses of the parametrically excited bimorph cantilever energy harvester constrained from both sides versus those constrained from one side; (a, b) maximum voltage and power outputs, respectively. R_l=5.0 kΩ, γ=2.0, g_0=42.0 mm, and a_x=9.81 m/s^2.

(a)

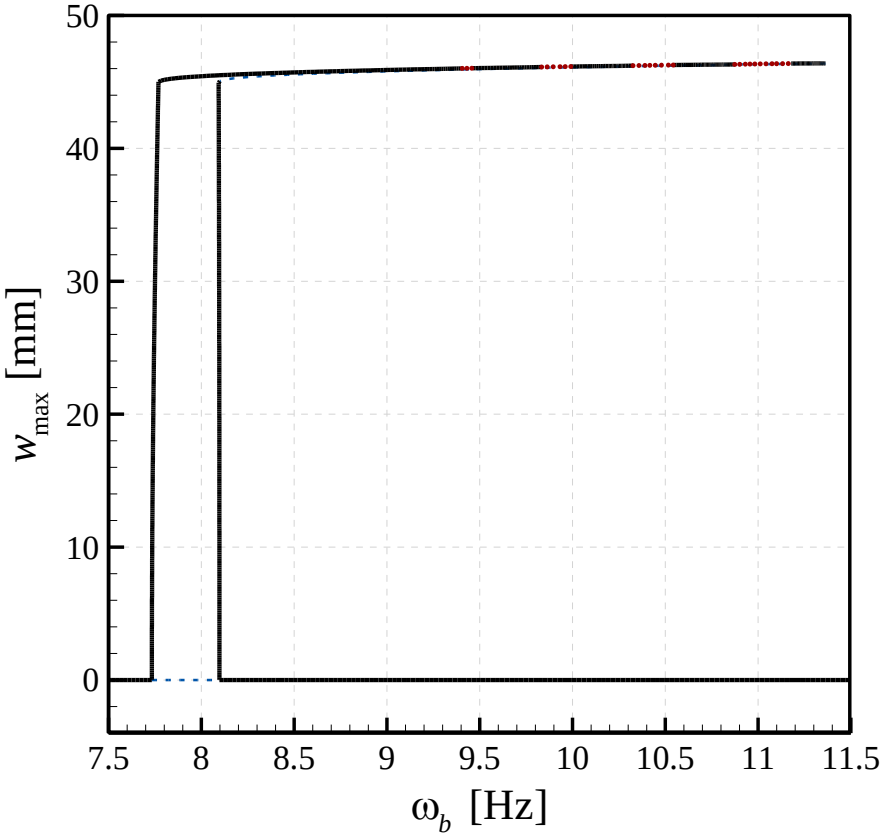
50
40
30
20
10
0
w_{max} [mm]
7.5
8
8.5
9
9.5
10
10.5
11
11.5
ω_b [Hz]

(b)

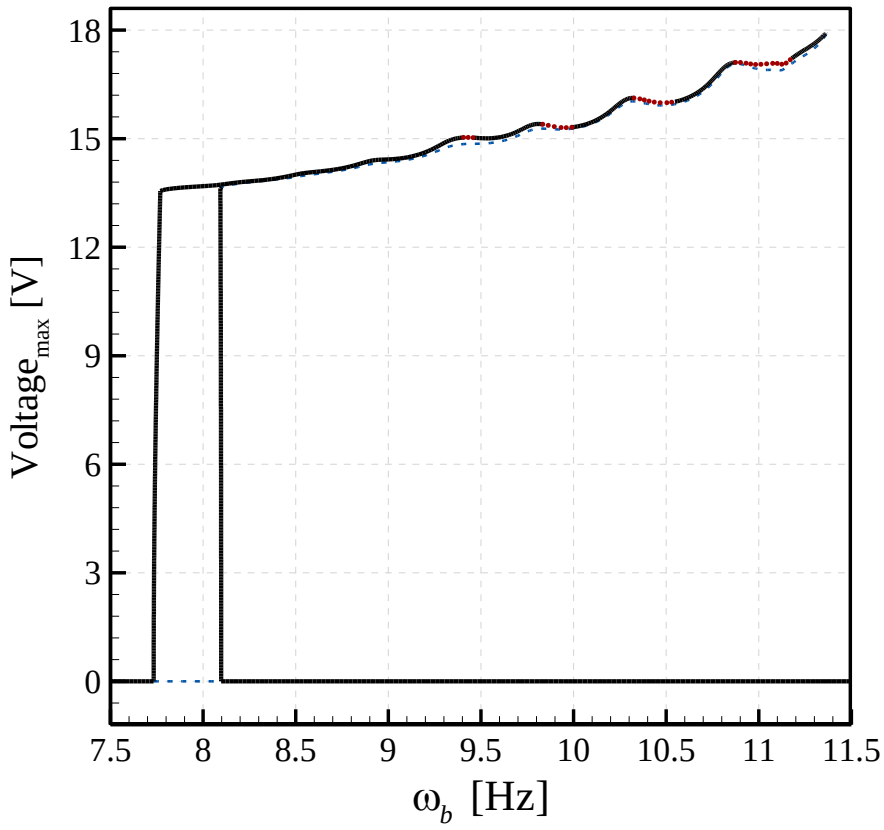
18
15
12
9
6
3
0
Voltage$_{max}$ [V]
7.5
8
8.5
9
9.5
10
10.5
11
11.5
ω_b [Hz]

(c)

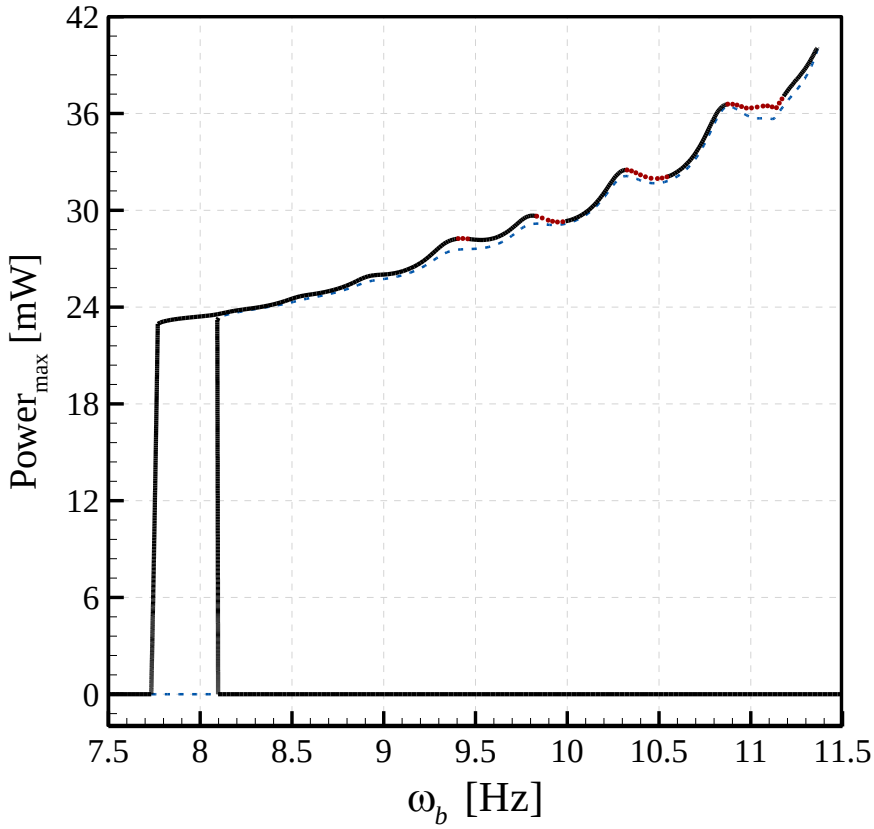

Fig.8. Frequency responses of the parametrically excited constrained bimorph cantilever energy harvester: (a) maximum tip transverse displacement; (b, c) maximum voltage and power outputs, respectively. R_l=8.0 kΩ, γ=3.0, g_0=45.0 mm, and a_x=9.81 m/s^2.

(a)

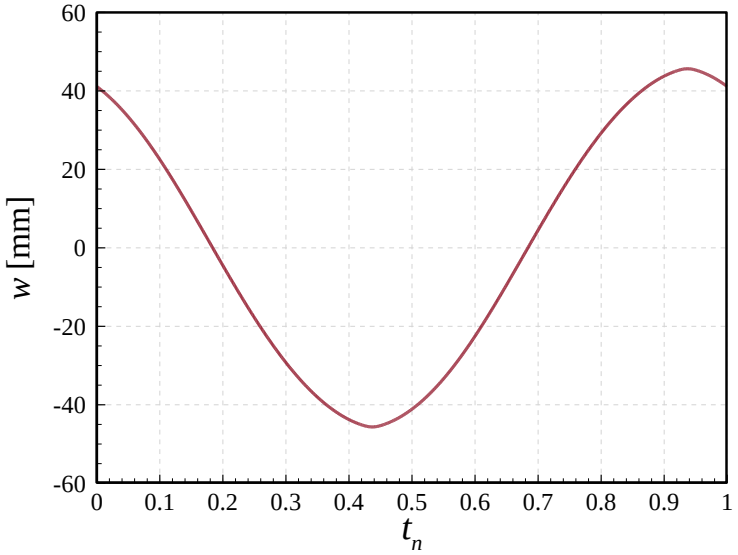

(b)

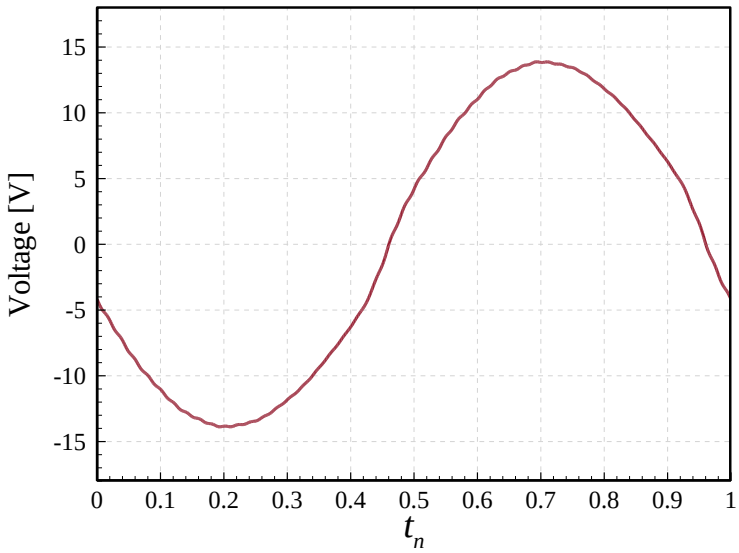

(c)

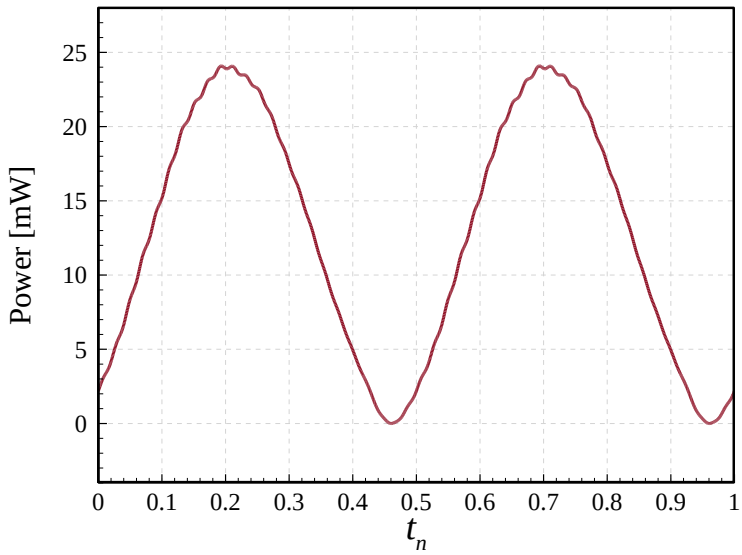

Fig.9. Response of the system of Fig. 8 at ω_b=8.3700 Hz; (a-c) tip transverse displacement, voltage output, and power output in one period of oscillation, respectively. t_n: normalised time.

(a)

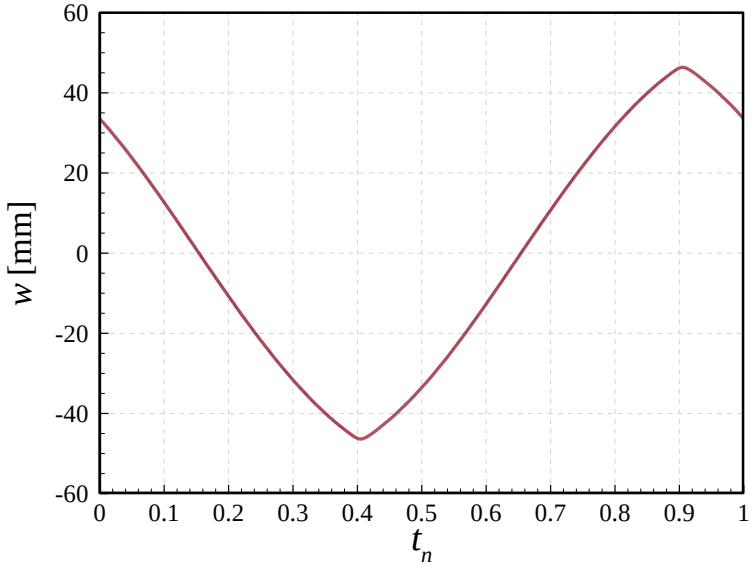

(b)

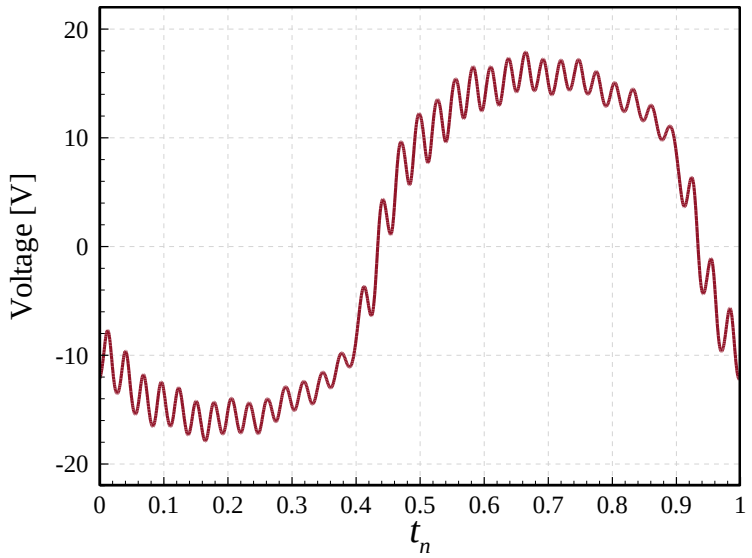

(c)

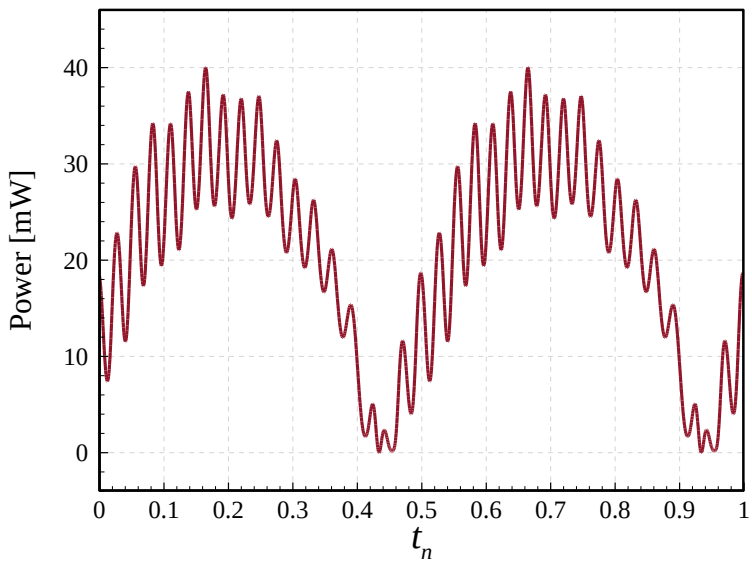

Fig.10. Response of the system of Fig. 8 at ω_b=11.3634 Hz; (a-c) tip transverse displacement, voltage output, and power output in one period of oscillation, respectively. t_n: normalised time.

(a)

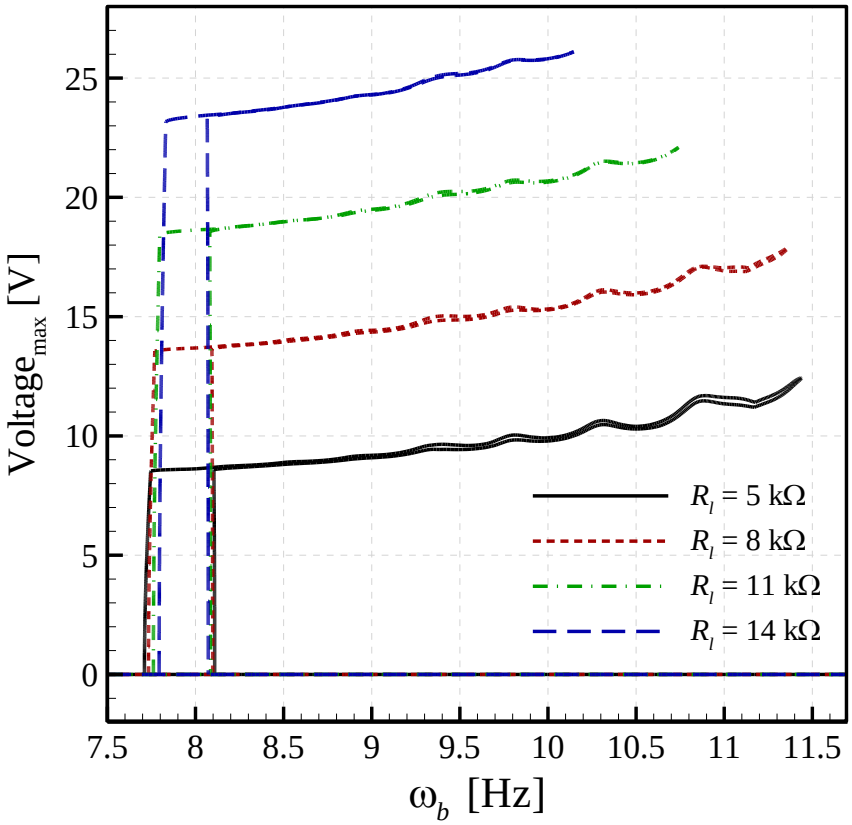

(b)

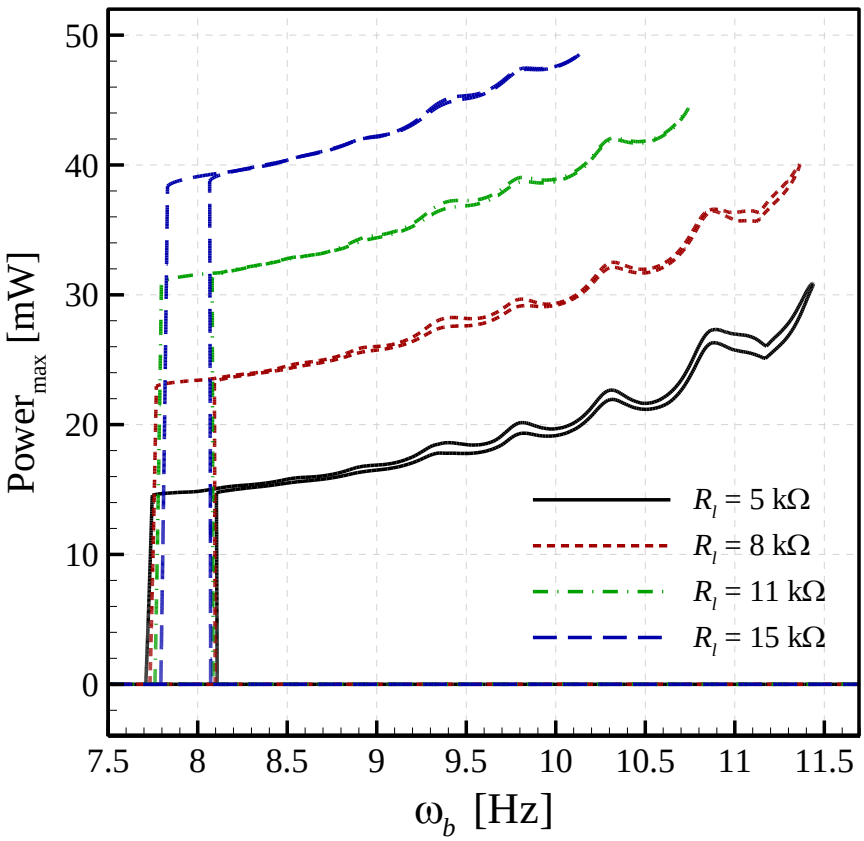

Fig.11. Load resistance effect on frequency responses of the parametrically excited constrained bimorph cantilever energy harvester: (a, b) maximum voltage and power outputs, respectively. γ=3.0, g_0=45.0 mm, and a_x=9.81 m/s^2.

(a)

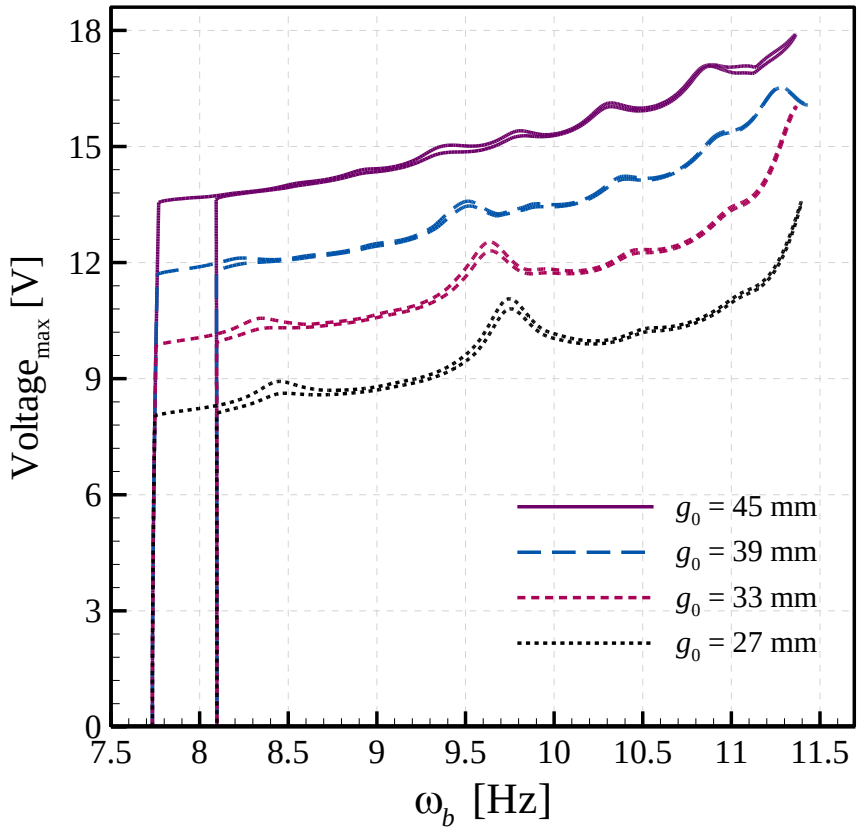

(b)

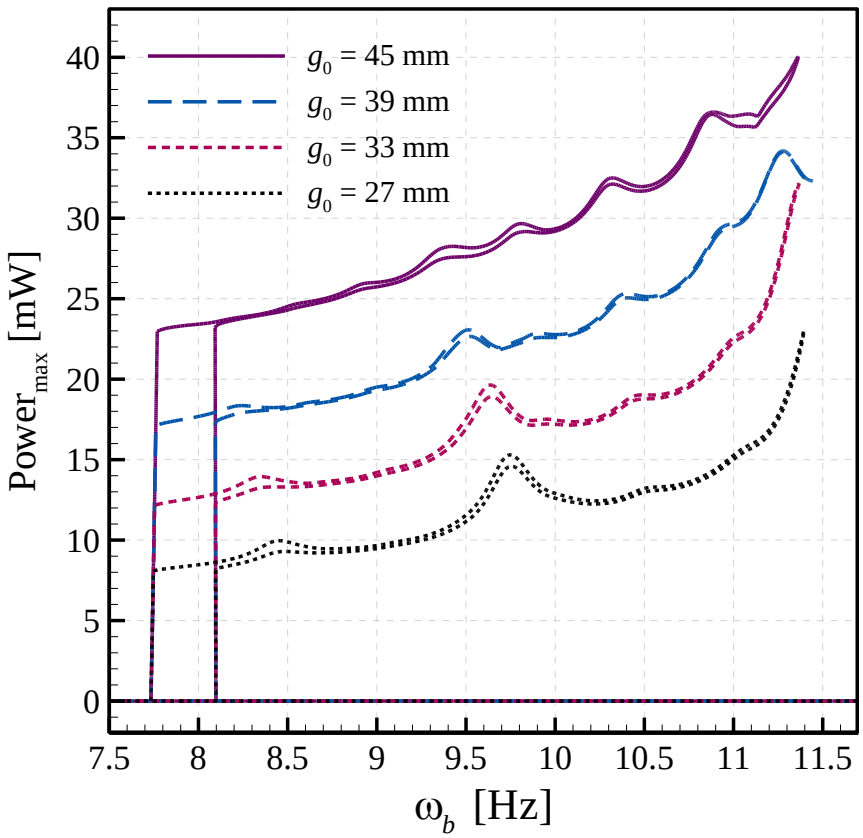

Fig.12. Gap effect on frequency responses of the parametrically excited constrained bimorph cantilever energy harvester: (a, b) maximum voltage and power outputs, respectively. R_l=8.0 kΩ, γ=3.0, and a_x=9.81 m/s^2.

(a)

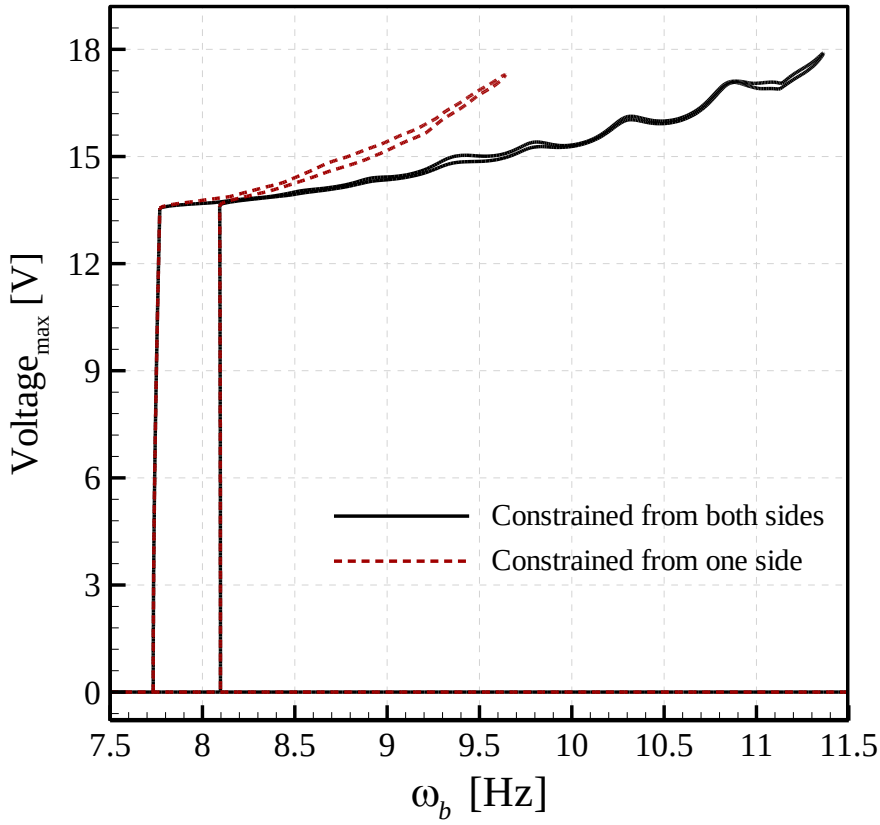

(b)

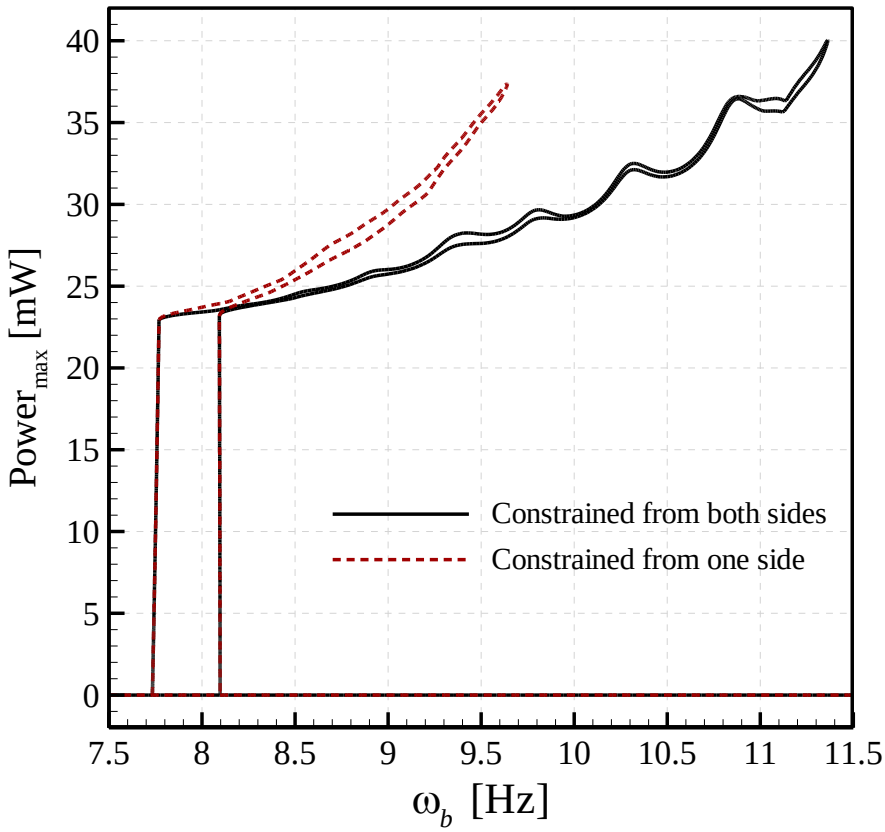

Fig.13. Frequency responses of the parametrically excited bimorph cantilever energy harvester constrained from both sides versus those constrained from one side; (a, b) maximum voltage and power outputs, respectively. R_l=8.0 kΩ, γ=3.0, g_0=45.0 mm, and a_x=9.81 m/s^2.

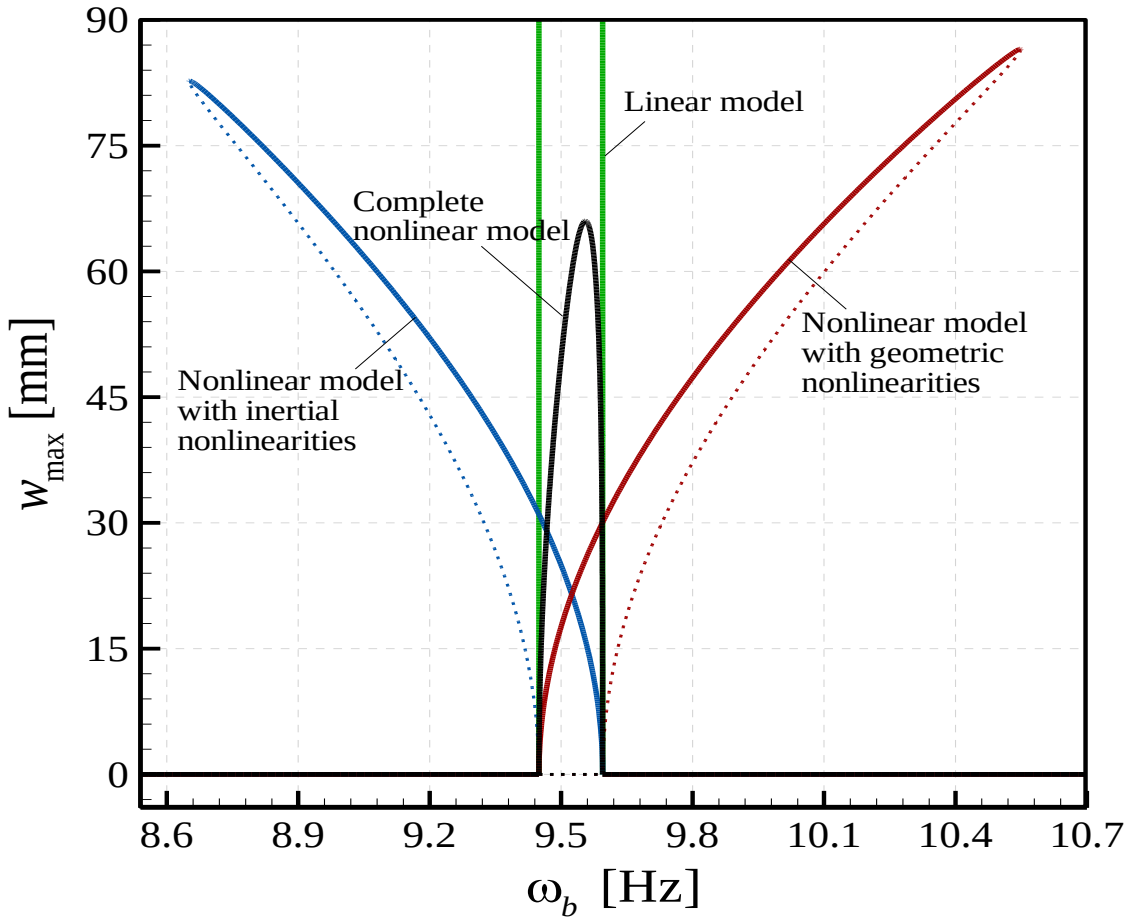

Fig.14. Frequency responses of the parametrically excited bimorph cantilever energy harvester obtained via different models.